Flow and Heat Transfer Across Trapezoidal Bluff Bodies

A DISSERTATION

Submitted in partial fulfillment of the
requirements for the award of the degree

of

MASTER OF TECHNOLOGY

in

CHEMICAL ENGINEERING

(with Specialization in Computer Aided Process Plant Design)

by

RITWIK GHOSH

DEPARTMENT OF CHEMICAL ENGINEERING
INDIAN INSTITUTE OF TECHNOLOGY ROORKEE
ROORKEE – 247 667 (INDIA)
June, 2013

Declaration

I hereby declare that the work presented in this dissertation entitled "**Flow and heat transfer across trapezoidal bluff bodies**" submitted towards partial fulfillment for the award of the degree of M.Tech. in Chemical Engineering with specialization in Computer Aided Process Plant Design at the Indian Institute of Technology, Roorkee is an authentic record of my original work carried out under the guidance of **Dr.A.K.Dhiman** (IIT Roorkee). I have not submitted the matter embodied in this dissertation for the award of any other degree.

Place:- Roorkee Ritwik Ghosh

Date:-15/06/2013Enrol. No.-11514017

Certificate

This is to certify that Mr. Ritwik Ghosh (Enrol. No.11514017) has completed the dissertation entitled "**Flow and heat transfer across trapezoidal bluff bodies**" under my supervision.

(**Dr.A.K.Dhiman**)
Assistant Professor
Dept. of Chemical Engineering
IIT Roorkee

Acknowledgements

I would like to express my sincere gratitude to my supervisor, Dr. A. K. Dhiman for his encouragement, guidance and support. I would also like to thank Dr. V. K. Agarwal (Head of the Department) and Dr. Surendra Kumar for providing me with the opportunity and the resources for my dissertation work. I would like to express my sincerest appreciation to my lab mates Alex Daniel, Deepak Kumar, Ram Parvesh Ram, Varun Mittal, Shishir Gupta and Vandana Gautam for creating a healthy environment to work in. I also take this opportunity to recognize the contribution of my friends specially Shubhradeep Moitra and Chand Kumar for their constant optimism. I would like to acknowledge the selfless support of my parents and Pooja for having utmost faith in me in whatever I did. Finally, I would like to thank all the teaching and non-teaching staff of Chemical Engineering Department for making my two years of M.Tech. a truly enriching educational experience.

Ritwik Ghosh

11514017

M.Tech.(C.A.P.P.D.)

Table of Contents

List of Figures

List of Tables

Abstract

Part 1: Steady and unsteady forced convection flow and heat transfer past a long expanded trapezoidal bluff body are investigated for the air as working fluid for Re = 1 – 150. The wake length increases as the Reynolds number increases in the steady flow regime ($1 \le \mathrm{Re} \le 47$). The transition from steady regime to unsteady regime occurs between Re = 47 and 48. The total drag coefficient decreases with the increasing value of the Reynolds number up to Re = 90 and thereafter it increases with Reynolds number. However, heat transfer as well as Strouhal number increase with the increasing value of the Reynolds number. The maximum augmentation in heat transfer for the expanded trapezoidal cylinder with respect to the tapered trapezoidal cylinder is found to be approximately 146%. On the other hand, pressure drop shows an enhancement of approximately 97% for the expanded trapezoidal cylinder when compared with the tapered one. Simple correlations of wake length, drag, average Nusselt number and Strouhal number with Reynolds number have also been established.

Keywords: Expanded trapezoidal cylinder; Reynolds number; Wake length; Drag; Nusselt number; Strouhal number and Pressure loss.

Part 2: The two-dimensional numerical simulation of non-Newtonian power-law fluids across a heated trapezoidal bluff body has been studied in an unconfined configuration. The range of physical parameters considered as Reynolds number (Re) = 1 - 40, power-law index (n) = 0.4 - 1.8 and Prandtl number (Pr) = 50. The flow and temperature fields are represented by streamline and isotherm patterns for varying values of Re and n. The individual and overall drag coefficients, recirculation length and Nusselt number are calculated for the above range of settings. It is found that the drag coefficient decreases for $1 \le \mathrm{Re} \le 15$ with increase in power-law index. However, for $20 \le \mathrm{Re} \le 40$, the drag coefficient increases with increase in power-law index. The recirculation length and average Nusselt number increase with increase in both Reynolds number and power-law index. Finally, simple empirical equation relating the average Nusselt number with the Reynolds number has been derived.

Key words: Power-law fluid;trapezoidalcylinder; wake length; drag; Nusselt number; streamline and isotherm contours.

Nomenclature

Part 1:

a	front side of an expanded trapezoidal cylinder, m
b	rear side of an expanded trapezoidal cylinder, m
c_p	specific heat of the fluid, J kg^{-1} K^{-1}
C_D	total drag coefficient ($=2F_D / \rho U_\infty^2 b$)
C_{DF}	friction drag coefficient ($=2F_{DF} / \rho U_\infty^2 b$)
C_{DP}	pressure drag coefficient ($=2F_{DP} / \rho U_\infty^2 b$)
C_{Drms}	RMS value of the drag coefficient
C_L	total lift coefficient ($=2F_L / \rho U_\infty^2 b$)
C_{Lrms}	RMS value of the lift coefficient
dP	pressure drop
f	vortex shedding frequency, s^{-1}
F_D	drag force per unit length of the cylinder, N m^{-1}
F_{DF}	friction drag force per unit length of the cylinder, N m^{-1}
F_{DP}	pressure drag force per unit length of the cylinder, N m^{-1}
F_L	lift force per unit length of the cylinder, N m^{-1}

h	local heat transfer coefficient, W m^{-2} K^{-1}
$\overline{h}$	average heat transfer coefficient, W m^{-2} K^{-1}
H	height of the computational domain, m
k	thermal conductivity of the fluid, W m^{-1} K^{-1}
L	length of the computational domain, m
L_r	wake or recirculation length, m
Nu	local Nusselt number (= hb/k)
$\overline{Nu}$	average Nusselt number (= $\overline{h}b/k$)
Nu_{rms}	RMS value of the average Nusselt number
p	pressure, Pa
Pr	Prandtl number (= $\mu c_p / k$)
Re	Reynolds number (= $\rho U_\infty b / \mu$)
St	Strouhal number (= fb / U_∞)
T	temperature, K
T_∞	temperature of the fluid at the inlet, K
T_w	constant wall temperature at the surface of the cylinder, K
t	time, s
U_∞	uniform velocity at the inlet, m s^{-1}
V_x	component of the velocity in the x-direction, m s^{-1}

V_y component of the velocity in the y-direction, m s^{-1}

x stream-wise coordinate, m

X_d downstream distance, m

X_u upstream distance, m

y transverse coordinate, m

Greek symbols

μ viscosity of the fluid, kg m^{-1} s^{-1}

ρ density of the fluid, kg m^{-3}

Part 2:

a rear side of a tapered trapezoidal cylinder, m

b front side of a tapered trapezoidal cylinder, m

c_p specific heat of fluid, J/kg. K

C_p Surface pressure coefficient

C_D total drag coefficient ($=\frac{2F_D}{\rho U_\infty^2 b}$)

C_{Df} friction drag coefficient

C_{Dp} pressure drag coefficient

C_L total lift coefficient

F_D drag force per unit length, N/m

h local heat transfer coefficient, $W/m^2.K$

$\overline{h}$ Average heat transfer coefficient, W/m^2.K

H height of the computational domain, m

I_2 second invariant of rate of deformation tensor, s^{-2}

k thermal conductivity of fluid, W/m.K

L Length of the computational domain, m

Lr wake length, m

m power-law consistency index, Pa.s^n

n power-law index

Nu local Nusselt number ($=\frac{hb}{k}$)

$\overline{Nu}$ Average Nusselt number

P pressure, N/m^2

Pe Peclet number (=RePr)

Pr Prandtl number ($=\frac{mC_p}{k}\left(\frac{U_\infty}{b}\right)^{n-1}$)

P_w local pressure at a point on the surface, N/m^2

P_∞ reference pressure far away from the cylinder, N/m^2

Re Reynolds number ($=\frac{\rho U_\infty^{2-n} b^n}{m}$)

s Surface area, m^2

T_∞ temperature of the fluid at the inlet, K

T_w^* constant wall temperature at the surface of the cylinder, K

t	time(= t^* /(b / $U\_$))
U_∞	uniform velocity at the inlet, m/s
u	component of the velocity in x direction (= $\frac{u^*}{U_\infty}$)
v	component of the velocity in y direction (= $\frac{v^*}{U_\infty}$)
x	stream-wise coordinate (= $\frac{x^*}{b}$)
X_d	down stream distance of the cylinder, m
X	upstream distance of the cylinder, m
y	transverse coordinate (= $\frac{y^*}{b}$)

Greek symbols

θ	temperature (= $\frac{(T^* - T_\infty)}{(T_w^* - T_\infty)}$)
μ	viscosity of the fluid, kg/m.s
ρ	density of the fluid, kg/m^3
ε	rate of strain tensor, s^{-1}
η	viscosity of the power-law fluid, Pa.s/k
ζ	body force, kg.m/s^2
τ	deviatoric stress tensor
σ	stress tensor

Superscripts

*	dimensional variable

Publications

International Journals:

1. A. Dhiman, R. Ghosh, 2013, Computer simulation of momentum and heat transfer across an expanded trapezoidal bluff body, Int. J. Heat Mass Transfer, 59: 338 - 352.
2. R. Ghosh, A. Dhiman, 2013, Non-Newtonian power-law fluid flow and heat transfer across a tapered trapezoidal bluff body at low Reynolds numbers, Numer. Heat Transfer Part A: Applications, Communicated.

International Conferences:

1. R. Ghosh, A. Dhiman, 2012, CFD Investigation of unsteady flow and heat transfer across a tapered trapezoidal cylinder, Proceedings of the Thirty Ninth National Conference on Fluid Mechanics and Fluid Power December 13-15, 2012, SVNIT Surat, Gujarat, India.
2. R. Ghosh, A. Dhiman, 2012, Numerical Simulation of Unsteady Unconfined Heat Transfer From a Trapezoidal Bluff Body, Proceedings of Asian Conference on Mechanics of Functional materials, December 5-8, 2012, IIT Delhi.
3. R. Ghosh, A. Dhiman, 2012, Effects of Prandtl number on the Heat Transfer across a Tapered Trapezoidal Cylinder, Proceedings of International Conference on Advances in Chemical Engineering, February 22-24, 2013, IIT Roorkee

CHAPTER 1

INTRODUCTION

Flow around bluff bodies in both steady and unsteady regimes has been investigated extensively due to its relevance in various engineering applications. The trapezoidal bluff body is a typical configuration of vortex shedding bodies mounted on vortex flow meters and is widely used in electronic cooling, heat exchange systems, offshore structures, probes and sensors, flow metering devices and so on. However, the primary application of trapezoidal bluff bodies is to design, construct and operate a vortex flow meter. A vortex flow meter is differential pressure gauze which is based on the flow across a trapezoidal bluff body, especially tapered in shape. The flow around such obstacles is more complicated than regular geometries and very limited information is available in the literature.

Pankanin [1] made a detailed analysis of the various methods of investigating phenomena of the vortex flow meter and observed that the bluff body most suitable for the design of this type of device is a sharp edged trapezoidal cylinder. Xing et al. [2] performed numerical simulations to optimize the bluff body shape for increasing the efficiency of a vortex flow meter and observed that the tapered trapezoidal shaped bluff body serves the purpose. Venugopal et al. [3] carried out experimental investigations on vortex flow meter with the differential wall pressure measurement method and concluded that the tapered trapezoidal bluff body used by them is optimum. Further, a detailed analysis of multiple surrogates for the shape optimization of bluff body-facilitating mixing has been carried out by Mack et al. [4] thereby explaining the importance of tapered configuration in cost reduction for the construction of surrogates. Also, a trapezoidal bluff body is used for the setting up of piezoelectric sensors as experimented and explained by Wang et al. [5]. Further, trapezoidal shape finds its use in the construction of a cathode array ultrasound probe used by medical science for diagnosis. Gee et al. [6] presented a novel technique for 3D ultrasound probe calibration. The principle of operation is that the beam is aligned with a set of coplanar wires strung across a rigid frame. The probe which is trapezoidal in shape is mounted on a precision-manufactured mechanical instrument which allows adjustment and measurement of their relative pose. The scan plane used and the imaging array is also trapezoidal in shape.

The present work is concerned with the flow and heat transfer around a long trapezoidal bluff body for power-law fluids.

1.1 **Bluff body flow**

A boundary layer separation is always experienced by a bluff body when a fluid flows past it. Behind this bluff body (here the bluff body being trapezoidal) very strong flow oscillations is observed in the wake region. A periodic flow motion will develop in the wake as a result of boundary layer vortex shedding from either side of the cylinder at certain Reynolds number range. This regular pattern of vortices in the wake is called a Karman vortex street which creates an oscillating flow at a discrete frequency. This oscillatory nature of the vortex shedding phenomenon can sometimes lead to adverse structural vibrations which are initiated due to the resonance of the frequencies. In order to understand the phenomenon properly a few terms are needed to be addressed in details which are as follows:

1.1.1 Flow Separation: When the boundary layer travels far enough against an adverse pressure gradient that the speed of the boundary layer relative to the object falls almost to zero, flow separation is said to occur [7- 8]. The fluid flow becomes detached from the surface of the object, and instead takes the forms of eddies and vortices. In aerodynamics, flow separation can often result in increased drag, particularly pressure drag which is caused by the pressure differential between the front and rear surfaces of the object as it travels through the fluid. For this reason much effort and research has gone into the design of aerodynamic and hydrodynamic surfaces which delay flow separation and keep the local flow attached for as long as possible. Examples of this include the fur on a tennis ball, dimples on a golf ball, turbulators on a glider, which induce an early transition to turbulent flow regime; vortex generators on light aircraft, for controlling the separation pattern; and leading edge extensions for high angles of attack on the wings of aircraft. The flow reversal is primarily caused by an adverse pressure gradient imposed on the boundary layer by the outer potential flow. The stream-wise momentum equation inside the boundary layer is stated as

$$u\frac{\partial u}{\partial s} = -\frac{1}{\rho}\frac{dp}{ds} + v\frac{\partial^2 u}{\partial y^2}$$

where s, y are stream-wise and normal coordinates. An adverse pressure gradient is when $dp/ds > 0$, which then can be seen to cause the velocity to decrease along and possibly go to zero if the adverse pressure gradient is strong enough [9].

1.1.2 Wake: A wake is the region of recirculating flow immediately behind a moving or stationary solid body, caused by the flow of surrounding fluid around the body. In fluid dynamics, a wake is the region of disturbed flow (usually turbulent) downstream of a solid body moving through a fluid, caused by the flow of the fluid around the body. In incompressible fluids (liquids) such as water, a bow wake is created when a watercraft moves through the medium; as the medium cannot be compressed, it must be displaced instead, resulting in a wave. As with all wave forms, it spreads outward from the source until its energy is overcome or lost, usually by friction or dispersion. The formation of these waves in liquids is analogous to the generation of shockwaves in compressible flow, such as those generated by rockets and aircraft traveling supersonic through air

1.1.3 Vortex Shedding: In fluid dynamics, vortex shedding is an oscillating flow that takes place when a fluid such as air or water flows past a cylindrical body at certain velocities, depending to the size and shape of the body. In this flow, vortices are created at the back of the body and detach periodically from either side of the body. The fluid flow past the object creates alternating low-pressure vortices on the downstream side of the object. The object will tend to move toward the low-pressure zone. The boundary layer separates from the surface forms a free shear layer and is highly unstable. This shear layer will eventually roll into a discrete vortex and detach from the surface (a phenomenon called vortex shedding). Another type of flow instability emerges as the shear layer vortices shed from both the top and bottom surfaces interact with one another. They shed alternatively from the cylinder and generate a regular vortex pattern (the Karaman vortex street) in the wake. The vortex shedding occurs at a discrete frequency and is a function of the Reynolds number.

1.1.4Aerodynamic Loading: In consistency with Newton's second law of motion it can be stated that an integration of the linear momentum inside a control volume surrounding the circular cylinder can provide information of the aerodynamic forces (lift and drag) acting on the cylinder. Consequently, there must be also an oscillatory up and down force acting periodically on the cylinder. This periodic forcing exerting on the cylinder body is responsible for the vortex-induced vibrations as described earlier.

1.1.5 Momentum Balance: This concept can be used to determine the external force acting on an object. Usually, there is a momentum deficit in the wake profile along the stream-wise direction as relative to the incoming momentum upstream of the object. Therefore, a simple balance of the momentum flow in and out of the control volume

surrounding the object suggests that there is net force acting on the object. This net force along the flow direction is called the drag. Averaged velocity profiles of the flow past a circular cylinder is provided as a general representation of the wake flow field. Selected profiles at several representative regions also presented for reference. Near the bluff body, flow separates from the surface. Immediately behind the bluff body, a recirculation region exists with a strong reversing flow. The region between the cylinder and the end of the recirculation region is called the vortex formation region. Further downstream, the two separating shear layers merge and the velocity profile presents a typical wake profile. It is clear that there is a deficit in the center of the wake. This deficit in the momentum flow is the direct result of drag force acting on the cylinder.

1.2 Power law fluids

A Power-law fluid, or the Ostwald–de Waele relationship, is a type of generalized Newtonian fluid for which the shear stress, τ, is given by

$$\tau = K\left(\frac{\partial u}{\partial y}\right)^n$$

Where K is the flow consistency index (Pa.s^n), $\partial u/\partial y$ is the shear rate or the velocity gradient perpendicular to the plane of shear (s^{-1}), and n is the flow behavior index (dimensionless).
The following quantity represents an apparent or effective viscosity as a function of the shear rate (Pa.s):

$$\mu_{eff} = K\left(\frac{\partial u}{\partial y}\right)^{n-1}$$

Also known as the Ostwald–de Waele power law, this mathematical relationship is useful because of its simplicity, but only approximately describes the behavior of a real non-Newtonian fluid. For example, if n were less than one, the power law predicts that the effective viscosity would decrease with increasing shear rate indefinitely, requiring a fluid with infinite viscosity at rest and zero viscosity as the shear rate approaches infinity, but a real fluid has both a minimum and a maximum effective viscosity that depend on the physical chemistry at the molecular level. Therefore, the power law is only a good description of fluid behavior across the range of shear rates to which the coefficients were fitted.

Power-law fluids can be subdivided into three different types of fluids based on the value of their flow behavior index:

n	**Type of fluid**
n<1	Shear-thinning fluids
n = 1	Newtonian fluids
n>1	Shear-thickening fluids

Shear-thinning fluids: Shear-thinning is an effect where a fluid's viscosity—the measure of a fluid's resistance to flow—decreases with an increasing rate of shear stress. Another name for a shear-thinning fluid is a pseudoplastic. This property is found in certain complex solutions, such as lava, ketchup, whipped cream, blood, paint, and nail polish. It is also a common property of polymer solutions and molten polymers. Pseudoplasticity can be demonstrated by the manner in which squeezing a bottle of ketchup, a Bingham plastic, causes the contents to undergo a change in viscosity. The force causes it to go from being thick like honey to flowing like water. The study of such phenomena is called rheology. All materials that are shear thinning are thixotropic, in that they will always take a finite time to bring about the rearrangements needed in the microstructural elements that result in shear thinning [10].A common household example of a strongly shear-thinning fluid is styling gel, which primarily composed of water and a fixative such as a vinyl acetate/vinylpyrrolidone copolymer (PVP/PA). If one were to hold a sample of hair gel in one hand and a sample of corn syrup or glycerine in the other, they would find that the hair gel is much harder to pour off the fingers (a low shear application), but that it produces much less resistance when rubbed between the fingers (a high shear application).

Newtonian fluids: In continuum mechanics, a fluid is said to be Newtonian if the viscous stresses that arise from its flow, at every point, are proportional to the local strain rate — the rate of change of its deformation over time [11 - 13] which is equivalent to saying that those forces are proportional to the rates of change of the fluid's velocity vector as one moves away from the point in question in various directions. More precisely, a fluid is Newtonian if, and only if, the tensors that describe the viscous stress and the strain rate are related by a constant viscosity tensor that does not depend on the stress state and velocity of the flow. If the fluid is also isotropic (that is, its mechanical properties are the same along any direction), the viscosity tensor reduces to two real coefficients, describing the fluid's resistance to

continuous shear deformation and continuous compression or expansion, respectively. Newtonian fluids are the simplest mathematical models of fluids that account for viscosity. While no real fluid fits the definition perfectly, many common liquids and gases, such as water and air, can be assumed to be Newtonian for practical calculations under ordinary conditions. Newtonian fluids are power-law fluids with a behavior index of 1, where the shear stress is directly proportional to the shear rate:

$$\tau = \mu\left(\frac{du}{dy}\right)$$

These fluids have a constant viscosity, μ, across all shear rates and include many of the most common fluids, such as water, most aqueous solutions, oils, corn syrup, glycerine, air and other gases. While this holds true for relatively low shear rates, at high rates most oils in reality also behave in a non-Newtonian fashion and thin. Typical examples include oil films in automotive engine shell bearings and to a lesser extent in gear-tooth contacts.

Shear-thickening fluids: A shear thickening fluid, also called a dilatant, is a Non-Newtonian fluid where the shear viscosity increases with applied shear stress. This behavior is only one type of deviation from Newton's Law, and it is controlled by such factors as particle size, shape, and distribution. The properties of these suspensions depend on Hamaker theory and Van der Waals forces and can be stabilized electrostatically or sterically. Shear thickening behavior occurs when a colloidal suspension transitions from a stable state to a state of flocculation. Such behavior is currently being researched for use in body armor applications by companies like Dow Corning with their Active Protection System. A large portion of the properties of these systems are due to the surface chemistry of particles in dispersion, known as colloids. This can readily be seen with a mixture of cornstarch and water, which acts in counterintuitive ways when struck or thrown against a surface. Sand that is completely soaked with water also behaves as a dilatant material. This is the reason why when walking on wet sand, a dry area appears underneath your foot. Rheopecty is a similar property in which viscosity increases with cumulative stress or agitation over time. The opposite of a dilatant material is a pseudoplastic.

CHAPTER – 2

LITERATURE REVIEW

The present work is concerned with the forced convection flow and heat transfer around unconfined trapezoidal cylinder (tapered and expanded) in both steady and unsteady regimes. It is hence useful to briefly review the previous works on the momentum and heat transfer around a cylinder of trapezoidal cross-section and the effects of physical parameters on flow and heat transfer characteristics.

Steggel and Rockliff [14] demonstrated the effect of after body geometry on the vortex shedding characteristics of bluff bodies by investigating the viscous flow around rectangles. They stated that the after body geometry has a significant effect on the shedding characteristics due to interaction of the rear edge of the body with the separated shear layer which is formed on the body and which oscillates as a result of the shearing at the rear edge. With longer bodies and with the ones with greater relative vertical dimension at the rear end, the presence of the body surface limits the oscillation and hence the possible lift force is generated. Similarly, Singha and Balachandra [15] investigated the coherent structure statistics in the wake of a sharp-edged bluff body placed vertically in a shallow channel and concluded that the wakes formed behind bluff bodies are found to contain a considerable number of coherent structures of both senses of rotation. The maximum size of the structures can be as big as twice the width of the bluff body.

Goujon-Durand et al. [16] experimentally investigated the vortex shedding from a trapezoidal bluff body. They obtained the scaling laws for the evolution of the global mode describing the envelope of the peak to peak amplitude velocity oscillation in the wake flow downstream of the body. Vortex emission behind cylinders with trapezoidal cross-section has been experimentally studied in air-water vertical two-phase flows by Hulin et al. [17] which is verified and analyzed by using optical fiber probe measurements. Lee [18] numerically studied the early stages of the symmetrical wake flow developments around a tapered trapezoidal cylinder for Re = 25 - 1000. The flow starts with no separation and the symmetrical standing zone of recirculation develops aft of a trapezoidal cylinder with the advancement of the time. Miau et al. [19] made a detailed study on the low-frequency fluctuations in the near-wake region of a trapezoidal cylinder with low aspect ratio at high Reynolds numbers. Chung and Kang [20] studied the Strouhal number from tapered

trapezoidal cylinders for Reynolds numbers of 100, 150 and 200 at varying height ratios (0.3 – 1). The Strouhal number has minimum values at height ratios of 0.7 and 0.85 for Reynolds numbers of 100 and 150, respectively. The movement of the flow separation point from the rear to front corners and the change of secondary vortex strength are important factors in determining the shedding structures. El Wahed et al. [21] performed a numerical study of vortex shedding from different shaped bluff bodies, of which tapered trapezoidal bluff body is one at high Reynolds numbers. They stated that the regular vortex shedding is rapidly achieved in the case of a tapered trapezoidal bluff body as compared to other obstacles. Kahawita and Wang [22] carried out the two-dimensional (2-D) numerical simulations of the Benard von Karman hydrodynamic instability behind trapezoidal bluff bodies. They reported that the influence of the trapezoidal height is the dominant on the value of Strouhal number, when compared with the effect of the smaller trapezoidal base width. Venugopal et al. [23] did experimental investigations on the vortex flow meter with the differential wall pressure measurement method. They demonstrated that the vortex flow meter comprising of a trapezoidal cross-section is one of the major contributors in the field of flow metering. The accuracy, reliability and rangeability are factors which place vortex flow meters ahead of other differential pressure devices. Recently, Dhiman and Hasan [24] investigated the fluid flow over a heated tapered trapezoidal cylinder in both steady and time-periodic regimes (Re = 1- 150) for air as working fluid. The onset of flow separation is observed to exist between Re = 5 and 6. The critical value of the Reynolds number (i.e., transition to periodic unsteady) exists between Re = 46 and 47. The drag coefficient is found to decrease with the increasing Reynolds number in the steady regime; however, the drag is observed to increase with Reynolds number in the unsteady regime. The Strouhal number and the average Nusselt number increase with the increasing value of the Reynolds number.

On an expanded trapezoidal bluff body, Lee [25] employed a stream function-vorticity formulation to describe the unsteady flow field for Re = 25 - 1000. Pressure contours, surface pressure coefficient and drag coefficient are studied through the streamline flow field. Main-flow and sub-flow regimes are identified through an analysis of the evolution of the flow characteristics. Chen et al. [26] performed the 2-D flow around a porous expanded trapezoidal cylinder. At large Darcy number, the Reynolds number has to be higher before the vortex shedding phenomena occurs and the fluctuation-amplitude of drag coefficient decreases. The effects of the stress jump parameters are provided for Reynolds number range 20 - 200. Recently, Dhiman and Ghosh [27] made a detailed analysis of the momentum and

heat transfer across an expanded trapezoidal bluff body. They stated that the wake length increases as the Reynolds number increases in the steady regime (1 Re 47). The transition from steady to time-periodic regime occurs between Re = 47 and 48. The total drag coefficient decreases with the increasing value of the Reynolds number up to Re = 90 and thereafter it increases with Reynolds number. However, heat transfer as well as Strouhal number increases with the increasing value of the Reynolds number.

Because no information is available on non-Newtonian momentum and heat transfer characteristics over a bluff body of trapezoidal cross-section, as far as we know, it is appropriate to briefly include non-Newtonian studies around other similar obstacles, e.g. square and triangular cylinders, in the unconfined domain. Evidently, sufficient information is accessible in the open literature on the flow around square and triangular bluff bodies at low Reynolds numbers. For instance, Dhiman et al. [28] studied the 2-D flow of power-law fluids over an isolated square cylinder for and, where n is the power-law index. The shear-thinning fluid behavior increases the drag above its Newtonian value; whereas, the shear-thickening behavior reduces the drag below its Newtonian value. Nevertheless, as the value of the Reynolds number is gradually increased, the role of power-law index diminishes. Subsequently, they [27] reported the forced convection heat transfer ($1 \le \mathrm{Pr} \le 100$) to power-law fluids from a heated square cylinder for the same range of settings as in [26]. Simple heat transfer correlations for estimating the value of mean heat transfer coefficient are derived. Moreover, they [28] investigated the steady mixed convection flow and heat transfer to Newtonian and power-law fluids from a heated square cylinder for Re = 1 - 30, n = 0.8 - 1.5 and Pr = 0.7 - 100. The effects of Prandtl number and of power-law index on the Nusselt number are found more prominent than that of buoyancy parameter for a fixed Reynolds number. Similarly, Paliwal et al. [29] studied the steady momentum and forced convection heat transfer of power-law liquids past a square cylinder for a range of rheological and kinematic conditions as Re = 5 – 40, n = 0.5 - 1.4 and Peclet number (Pe) = 5 - 400. However, these computations have been performed by using uniform grid structure. Likewise, for the case of a triangular bluff body, excellent momentum and heat transfer results in the unconfined domain can be found elsewhere [30]. Prhashanna et al. [30] stated that the effect of power-law index gradually diminishes with the increasing Reynolds number for shear-thinning fluids (n<1) at low Reynolds numbers ($1 \le \mathrm{Re} \le 30$). Shear-thinning behaviour is seen to promote heat transfer under otherwise identical conditions, thereby

making it possible to achieve 50 – 60% increase in heat transfer over and above that in Newtonian fluids.

Thus, to the extent we know and based on the above discussion, no work is reported on power-law fluid flow and heat transfer over a long trapezoidal bar besides having numerous engineering applications. Accordingly, the aim of this study is set to fill this gap in the literature and to investigate the momentum and heat transfer across a trapezoidal bluff body for power-law fluids in the range of Reynolds number and power-law index (thereby including shear-thinning, Newtonian and shear-thickening behaviours) for a Prandtl number of 50. The value of Prandtl number up to around 50 are severally dealt in chemical, petroleum, oil and gas industries in the processing of organic fluids like glycols, glycerols, and petroleum fractions. Moreover, due to high viscosity of such process streams, the Reynolds numbers are not high [31 - 33].

CHAPTER – 3

PROBLEM STATEMENT AND METHODOLOGY

The work has been divided into the following two parts:

Part 1: Momentum and heat transfer across an expanded trapezoidal bluff body

Part 2: Non-Newtonian power-law fluid flow and heat transfer across a tapered trapezoidal bluff body at low Reynolds numbers

3.1. Problem statement and governing equations

Part 1: The 2-D, incompressible and laminar flow (flowing from left to right) across a long expanded trapezoidal cylinder (rear face width, b = 1, front face width, $a = 0.5\,b$ and cylinder height in axial direction, b = 1) is considered in an unconfined domain, as shown in Fig. 1. At the inlet, the flow is uniform and isothermal with a velocity, U_∞ and a temperature, T_∞. The trapezoidal cylinder is maintained at a constant temperature of T_w^* ($> T_\infty$). The upstream distance from the inlet plane to the front surface of the trapezoidal cylinder (X_u) is set as $12\,b$ and the downstream distance between the rear surface of the trapezoidal cylinder and the exit plane (X_d) is taken as $22\,b$, with the total length of the computational domain (L) of $35\,b$ in the axial direction. The height of the computational domain (H) is used as 30 b in the lateral direction. These distances are chosen after a thorough numerical study and the details are provided below in this section after boundary conditions.

The governing continuity, x- component and y- component of Navier-Stokes, and thermal energy equations in their dimensionless form for the present system as stated by Bird et al. [36] can be written as:

Continuity equation

$$\frac{\partial V_x}{\partial x} + \frac{\partial V_y}{\partial y} = 0 \tag{1}$$

x-Momentum equation

$$\frac{\partial V_x}{\partial t} + \frac{\partial (V_x V_x)}{\partial x} + \frac{\partial (V_y V_x)}{\partial y} = -\frac{\partial p}{\partial x} + \frac{1}{\mathrm{Re}}\left(\frac{\partial^2 V_x}{\partial x^2} + \frac{\partial^2 V_x}{\partial y^2}\right) \tag{2}$$

y-Momentum equation

$$\frac{\partial V_y}{\partial t}+\frac{\partial (V_x V_y)}{\partial x}+\frac{\partial (V_y V_y)}{\partial y}=-\frac{\partial p}{\partial y}+\frac{1}{\mathrm{Re}}\left(\frac{\partial^2 V_y}{\partial x^2}+\frac{\partial^2 V_y}{\partial y^2}\right) \tag{3}$$

Energy equation

$$\frac{\partial \theta}{\partial t}+\frac{\partial (V_x \theta)}{\partial x}+\frac{\partial (V_y \theta)}{\partial y}=\frac{1}{\mathrm{Re}\,\mathrm{Pr}}\left(\frac{\partial^2 \theta}{\partial x^2}+\frac{\partial^2 \theta}{\partial y^2}\right) \tag{4}$$

In equations (1) – (4), the Reynolds and Prandtl numbers are defined as $\mathrm{Re}=bU_\infty \rho/\mu$ and $\mathrm{Pr}=\mu c_p/k$, respectively.

The boundary conditions (in their dimensionless form) for the unconfined flow and heat transfer across a heated expanded trapezoidal cylinder can be written as

- *At the inlet boundary*, $V_x=1$, $V_y=0$ and $\theta=0$
- *On upper and lower boundaries*, $\partial V_x/\partial y=0$, $V_y=0$ and $\partial\theta/\partial y=0$
- *On the surface of the trapezoidal obstacle*, $V_x=0$, $V_y=0$ and $\theta=1$
- *At the exit boundary*, $\partial V_x/\partial x=0; \partial V_y/\partial x=0$ and $\partial\theta/\partial x=0$

The governing equations (1 - 4) along with above noted boundary conditions are solved by using a finite volume solver Ansys Fluent [37].

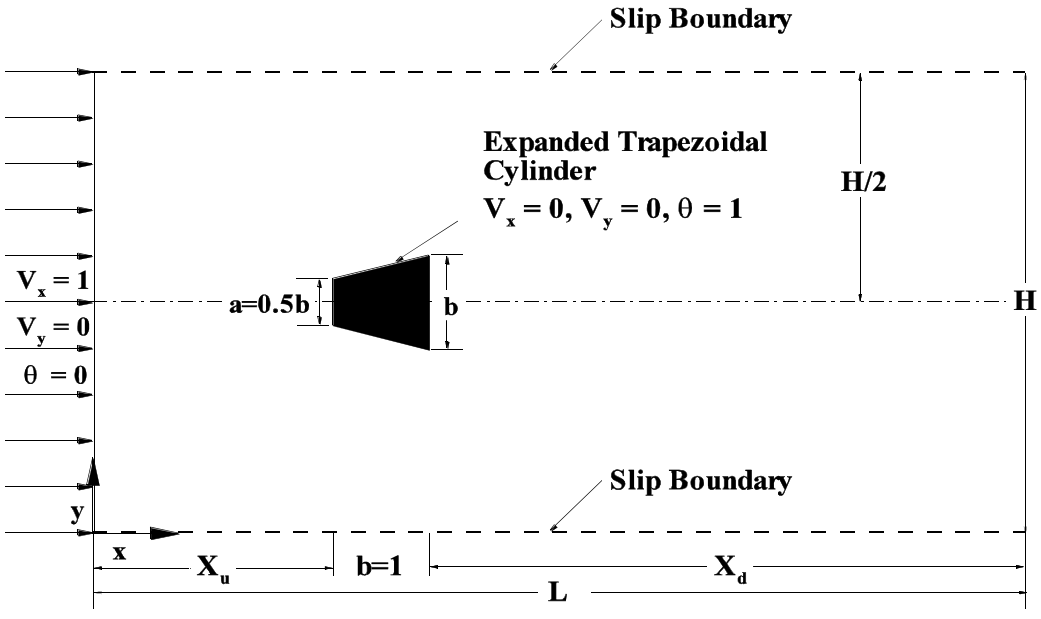

Figure 1: *Schematics of the flow around an expanded trapezoidal cylinder in the unconfined domain*

The second order upwind scheme is used to discretize convective terms; whereas, the diffusive terms are discretized by central difference scheme. The second order implicit time-integration method is used here and the dimensionless time step is set to 0.01. To determine the optimum value of the time step, three values of the time step (0.1, 0.01 and 0.005) are studied at Re = 150. The relative difference in the values of physical parameters (drag, Nusselt and Strouhal numbers) is observed about 2.9%. While the corresponding difference in the values is found less than 0.5%. The resulting algebraic equations are solved by Gauss-Siedel iterative scheme. The residuals of the continuity, x- and y- momentums and energy equations are used of the order of 10^{-10} in the steady regime and of the order of 10^{-20} each in the unsteady regime.

Part 2: The two-dimensional unconfined laminar flow and heat transfer characteristics have been determined for power-law fluids around a long tapered trapezoidal obstacle. The schematics of the present flow system are presented in Fig. 2. The fluid flowing from left to right is uniform and isothermal with a velocity U_∞ and a temperature T_∞ at the inlet. The tapered trapezoidal cylinder is maintained at a constant temperature of $T_w^* (> T_\infty$).The upstream distance (X_u) is 12b, downstream distance (X_d) is 20b and the height of the computational domain (H) is 30b in the lateral direction. The front face width of a trapezoidal cylinder (b)= 1, rear face width (a) = 0.5b, and cylinder height (b) = 1 with the total length of the computational domain (L) = 33b in the axial direction are used in this work. These values are decided after a thorough investigation.

For an incompressible, 2-D and laminar flow, the dimensionless form of the continuity equation, the x- component and y-component of Cauchy's equation and thermal energy equation as stated by Bird et al. [36] are given below:

Continuity equation:

$$\frac{\partial u}{\partial x} + \frac{\partial v}{\partial y} = 0 \tag{5}$$

x- Momentum equation:

$$\frac{\partial u}{\partial t} + u\frac{\partial u}{\partial x} + v\frac{\partial u}{\partial y} = -\frac{\partial p}{\partial x} + \frac{1}{\mathrm{Re}}\left(\frac{\partial \tau_{xx}}{\partial x} + \frac{\partial \tau_{yx}}{\partial y}\right) \tag{6}$$

y- Momentum equation:

$$\frac{\partial v}{\partial t} + u\frac{\partial v}{\partial x} + v\frac{\partial v}{\partial y} = -\frac{\partial p}{\partial y} + \frac{1}{\mathrm{Re}}\left(\frac{\partial \tau_{yy}}{\partial x} + \frac{\partial \tau_{xy}}{\partial y}\right) \tag{7}$$

Energy equation:

$$\frac{\partial \theta}{\partial t} + u\frac{\partial \theta}{\partial x} + v\frac{\partial \theta}{\partial y} = \frac{1}{Pe}\left(\frac{\partial^2 \theta}{\partial x^2} + \frac{\partial^2 \theta}{\partial y^2}\right) \tag{8}$$

The power-law fluid behaviour is represented by

$$\tau_{ij} = 2\eta\varepsilon_{ij} \qquad (i, j = x, y) \tag{9}$$

and

$$\eta = (I_2 / 2)^{(n-1)/2} \tag{10}$$

where

$$I_2 / 2 = 2\left(\frac{\partial u}{\partial x}\right)^2 + 2\left(\frac{\partial u}{\partial y}\right)^2 + \left(\frac{\partial u}{\partial y} + \frac{\partial v}{\partial x}\right)^2 \tag{11}$$

In this study, thermo-physical properties of the streaming fluid are assumed to be independent of the temperature. The viscous dissipation and the buoyancy effects are also neglected such that the present work is applicable to situations where the temperature difference is not too large and for moderate viscosity and/or shearing levels.

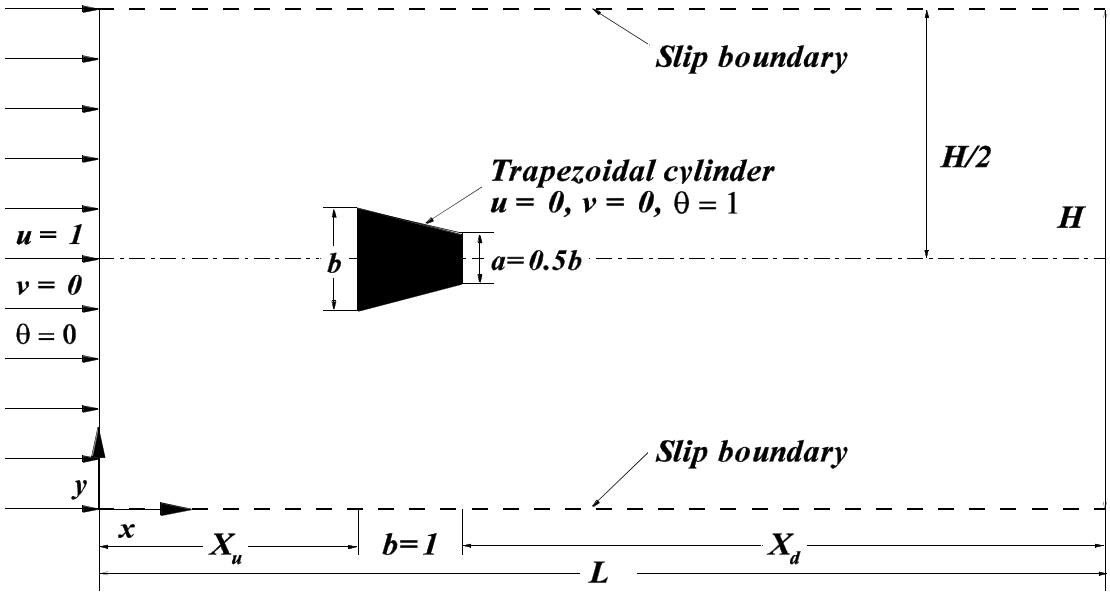

Figure 2: *Schematic diagram for unconfined flow around a heated tapered trapezoidal bluff body*

The boundary conditions in their dimensionless form can be written as: At the inlet boundary: $u = 1,\ v = 0$ and $\theta = 0$;On upper and lower boundaries: $\partial u / \partial y = 0$, $v = 0$ and $\partial \theta / \partial y = 0$;On the surface of a trapezoidal bluff body: $u = 0$, $v = 0$ and $\theta = 1$; and At the exit boundary: $\partial u / \partial x = 0,\ \partial v / \partial x = 0$ and $\partial \theta / \partial x = 0$. The continuity, the x- and y-components of Cauchy's equation and thermal energy equation along with above noted boundary conditions are solved by using a finite volume method based commercial solver Ansys Fluent [37].

3.2. Numerical methodology

Part 1: The computational grid structure used in this work is generated by using Ansys workbench, as shown in Fig. 3. The grid consists of 123848 quadrilateral cells with each side of the expanded trapezoidal cylinder having 100 control volumes. A very fine grid of cell size of $0.004\,b$ is used around the obstacle; however, the largest grid size of $0.4\,b$ is used away from the obstacle. Three non-uniform grids (55348 cells, 123848 cells and 220206 with 50, 100 and 150 control volumes, respectively on each side of the cylinder) are tested for the grid dependence study for Re = 150 and Pr = 0.7. The percentage deviations in the values of the mean drag coefficient, average cylinder Nusselt number and Strouhal number for the grid size of 123848 cells are found to be about 2.1 %, 1.7 % and 1.5 %, respectively as compared to the values for the grid size of 55348 cells. However, the corresponding differences for 220206 cells are only 0.6 %, 0.3 % and 0.5 %, respectively as compared to the values for the grid size of 123848 cells. Therefore, the grid size of 123848 cells is found appropriate to generate further results in the present study.

The upstream dependence is checked at three values of upstream distances of $10\,b$, $12\,b$ and $14\,b$ at Re = 1. The relative percentage deviations in the values of total drag coefficient and average cylinder Nusselt number are found to be less than 1.9% and less than 1.5%, respectively for $X_u = 12\,b$ as compared to the values of the total drag coefficient and the average cylinder Nusselt number at $X_u = 10\,b$ for $X_d = 22\,b$ and H = 30b. The corresponding deviations in the values of total drag coefficient and average cylinder Nusselt number are found to be less than 0.6% and less than 0.4% for $X_u = 12\,b$ and $14\,b$ .Therefore, the upstream distance of $12\,b$ is used in this study.

Similarly, three values of downstream distances of $20\,b$, $22\,b$, and $25\,b$ are being used to fix the downstream distance and the study is carried out at Re = 150. The relative differences in the values of overall drag coefficient and average cylinder Nusselt number are

found to be less than 1.6% and less than 1.2%, respectively for $X_d = 22b$ and $20b$. However, the corresponding differences in the values of total drag and average cylinder Nusselt number are found to be less than 0.3% and less than 0.1%, respectively for $X_d = 22b$ and $25b$. Thus, the downstream distance of $22b$ is found adequate for the generation of results.

The height of the computational domain is fixed by varying the value of the domain height (H) from $20b$ to $30b$ for Re = 1, 100 and 150. The percentage deviations in the values of the total drag coefficient and the average cylinder Nusselt number are found to be about 3.4 % and 1.3 %, respectively for the domain height of $20b$ as compared to the values of 30 b for the Reynolds number of unity. For Re = 100, the corresponding percentage deviations in the values of mean drag coefficient, average cylinder Nusselt number and Strouhal number are found to be only about 0.3 %, 0.4 % and less than 0.4 %, respectively. However, for Re = 150, the corresponding percentage deviations in the values of mean drag coefficient, average cylinder Nusselt number and Strouhal number are found to be only about 0.5 %, 0.2 % and 0.7 %, respectively. Thus, the height of the computational domain of $30b$ is utilized here.

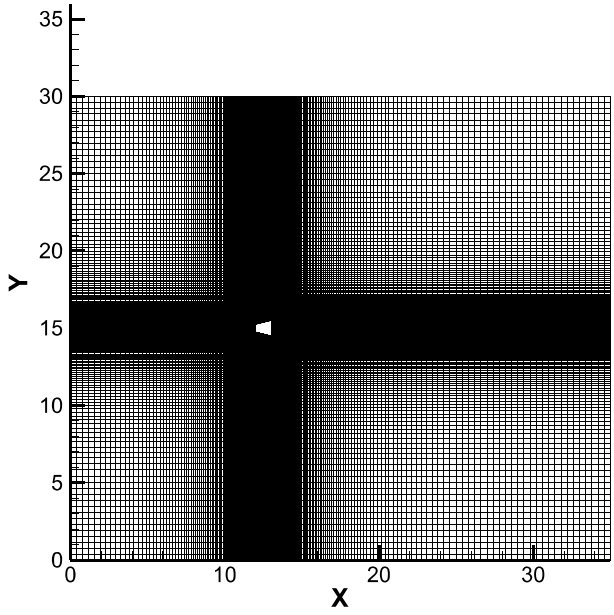

Figure 3: *Non-uniform computational grid structure around an expanded trapezoidal cylinder*

Part 2: In the current framework, the identical non-uniform grid structure used in our recent study [24] is utilized for the generation of new results. Briefly, the computational grid

consists of 1,20,520 cells (with each side of a trapezoidal cylinder having 100 control volumes) with a very fine grid of cell size of $0.004b_1$ near the obstacle and the largest grid size of $0.4b_1$ away from the obstacle is found adequate. The 2-D, steady/unsteady, laminar, segregated solver module of Ansys Fluent [37] is used to solve the incompressible flow on the collocated grid arrangement.

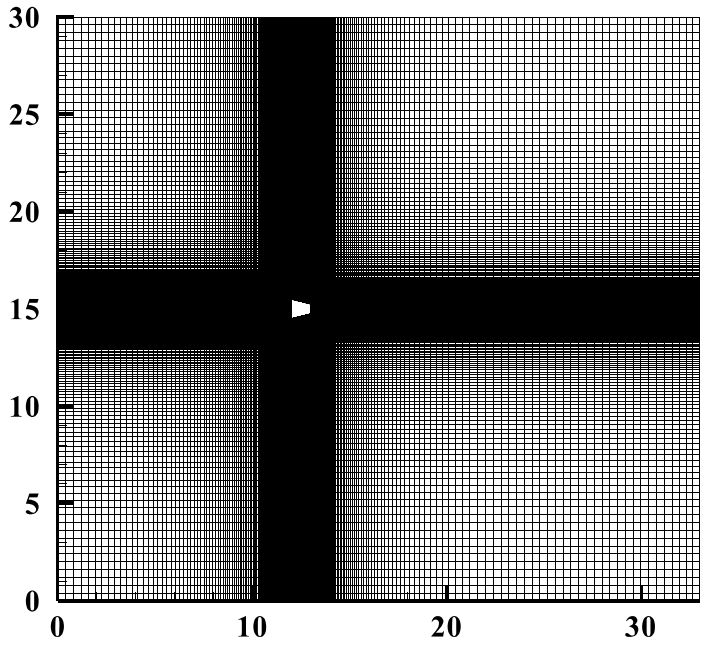

Figure 4: *Non-uniform computational grid around a tapered trapezoidal bluff body*

In addition, constant density and non-Newtonian power-law viscosity modules are used. The second order upwind scheme is used to discretize convective terms; whereas, the diffusive terms are discretized by central difference scheme. The second order implicit time-integration method is also used and the dimensionless time step is set to 0.01 as the smaller value of the time step produced negligible changes in the values of the physical parameters considered. The resulting algebraic equations are solved by Gauss-Siedel iterative scheme and the residual of continuity, the x- and y- components of velocity are used of the order of 10^{-10} in the steady regime and of 10^{-20} each in the time-periodic regime. Similar to [24], the upstream and downstream distances of $12b$ and $20b$ respectively in the axial direction, and the domain height of $30b$ in the lateral direction are found adequate in this work. The computational domain used for the present study has also found to be consistent with the experimental set up of Venugopal et al. [23] for the flow around a tapered trapezoidal cylinder, where the

upstream and downstream distances are fixed at 25b and 15b respectively. Nevertheless, Venugopal et al. [23] conducted their study for Re ranging from 1.1×10^5 to 3×10^5 and the present results are limited to low Reynolds numbers.

CHAPTER – 4

RESULTS AND DISCUSSION

Part 1: In the present numerical investigation, forced flow and heat transfer around a long expanded trapezoidal cylinder are examined systematically in both steady and unsteady regimes for Re = 1 – 150 (in the intervals of 10) for the air as working fluid (Pr = 0.7). The additional calculations are also carried out to determine the transition from steady to time-dependent regime. The various engineering parameters such as drag and lift coefficients, Strouhal number, local and average Nusselt numbers and pressure drop are calculated for the above range of settings. The representative streamline and isotherm contours are provided to understand the flow and thermal structures around the expanded cylinder under consideration. The results thus obtained after numerical simulations have been compared with the reliable results available in the literature and also compared with square and tapered trapezoidal cylinders.

Part 2: This section provides the details of numerical computations, which have been performed to investigate the momentum and heat transfer around a long trapezoidal bluff body in the unconfined domain, for Reynolds number (Re) = 1 - 40, power-law index (n) = 0.4 - 1.8 and Prandtl number (Pr) = 50. The global quantities like drag coefficient, wake length and Nusselt number are evaluated for shear-thinning (n< 1), Newtonian (n = 1) and shear-thickening (n> 1) liquids. The results thus obtained have been compared with the reliable results available in the literature and also compared with that of a long square bluff body. The maximum augmentation in heat transfer is calculated for the present flow system as well as with respect to a square cylinder. In the end, simple empirical equations relating the average Nusselt number with Reynolds number and power-law index are derived. These simple expressions can also be utilized to determine the intermediate values of the average Nusselt numbers in the range of settings covered in the present study.

4.1 Validation/Benchmarking of results

Part 1: The validation of present numerical methodology is made with the limited results of Chen et al. [26] and Lee [25] on the expanded trapezoidal cylinder. In the present study, the dimensionless wake length is found to be about 1.21 and this is in line with the results of Chen et al. [26] of 1.19 at the Reynolds number of 20. Therefore, an excellent agreement exists between present results and that of Chen et al. [26]. However, when a

comparison is made between the present results to that of Lee [25], it has been observed that a significant deviation exists between the two studies. For instance, while the drag coefficient is found to be about 1.12 from the results of Lee [25] at the Reynolds number of 50, the present results recorded it to be about 1.39 for the same value of the Reynolds number. The prime reason behind this is that the grid size used by Lee [25] for the computation is much coarse (19481 cells) than that used for present study (123848 cells). Also, the domain of study for Lee [25] is around one-third of that of the present study. In addition, the inconsistency in the numerical results is due to modeling error, discretization error, numerical error and accuracy of the scheme as explained by Roache [38].

Table 1: *Validation of the present results of Drag coefficient (C_D) and Strouhal number (St) with the literature values for unsteady unconfined flow regime at Re = 100*

Source	**C_D**	**% Deviation of C_D**	**St**	**% Deviation of St**
Present work	1.3045	-	0.1610	-
Patnana et al. [39]	1.3409	2.71	0.1657	2.84
Baranyi [41]	1.3460	3.08	0.1630	1.23
Cheng et al. [42]	1.3200	1.17	-	-
Mettu et al. [43]	1.3020	0.19	0.1600	0.62
Henderson [44]	1.3490	3.30	-	-
Sivakumar et al. [45]	1.3250	1.55	0.1641	1.89
Mittal [46]	1.3220	1.32	0.1644	2.07
Clift et al. [47]	1.3300	1.92	0.1670	3.59
Ding et al. [48]	1.3250	1.55	0.1640	1.83
Liu et al. [49]	1.3500	3.37	0.1640	1.83

Since an anomaly exists between the present results and that of Lee [25], the present work has been validated with Patnana et al. [39 - 40] for the fluid flow and heat transfer

across a cylinder at a high value of Reynolds number (Re) = 100 (Tables 1 and 2). The maximum deviations in the values of physical parameters like drag coefficient (C_D), Strouhal number (St) and Nusselt number (Nu) have been observed to be as low as about 2.71%, 2.84% and 0.95%, respectively. Tables 1 and 2 also illustrate the comparison of present results with the literature values [41 - 53] and the percentage deviations for each of the physical parameters analyzed. This validates the present numerical solution procedure.

Table 2: *Validation of the present results with the literature values of Nusselt number (Nu) for unsteady unconfined flow regime at Re = 100*

Source	Nu	% Deviation of Nu
Present work	5.1042	-
Patnana et al. [40]	5.1530	0.95
Baranyi [41]	5.1320	0.54
Karniadakis [50]	5.1529	0.95
Mahfouz and Badr [51]	5.3100	3.88
Lange et al. [52]	5.1280	0.46
Whitaker [53]	5.2600	2.96

Part 2: The benchmarking of present Newtonian results on a tapered trapezoidal bluff body is carried out in our recent study [24] and hence it is not reported. Similarly, the present numerical methodology has been benchmarked in [24] for the flow across a heated expanded trapezoidal cylinder in the unbounded configuration. Because no work is available for non-Newtonian flow and heat transfer across a trapezoidal bluff body, the computations have been carried out for the unconfined circular cylinder and validated with the numerical results of Sivakumar et al. [54] and Bharti et al. [55] for extreme values of Re and n at Pr = 50. The values of drag coefficients for n = 0.6, 1 and 1.8 are found to have a deviation of about 0.51%, 0.48% and 0.30%, respectively at Re = 1, and only about 0.09%, 0.01% and 0.07%, respectively at Re = 40. Correspondingly, the average Nusselt numbers for n = 0.6, 1 and 1.8

are found to have a deviation of about 0.28%, 1.22% and 0.01% respectively at Re = 1, and about 0.34%, 1.01% and 1.02% respectively at Re = 40.

4.2. Flow patterns

Part 1: The flow pattern is represented by streamline contours around the long expanded trapezoidal cylinder in both steady and unsteady regimes. Streamline contours are a group of constant velocity lines in the domain of present study which help in the analysis of fluid flow characteristics and also in identifying the nature of flow (i.e. steady or unsteady). Figures 5 (a-d) display the streamline contours in the vicinity of the expanded trapezoidal cylinder in the steady regime (Re = 1, 10, 20 and 40). On the other hand, in the time-dependent regime, Fig. 6 (a-l) exhibits the instantaneous streamline contours at different values of Reynolds numbers.

In utter contrast to the nature of the flow separation for the tapered trapezoidal cylinder [24], where the onset of flow separation occurs between Re = 2 and 3, the flow separation for the expanded trapezoidal bluff is observed below Re = 1. Further, if a comparative study is carried out for the flow past an expanded trapeze and that for a square block [28, 57], it is observed that flow separation occurs earlier for the expanded trapezoidal cylinder than the square block. This is due to the fact that the separation of flow in the case of a tapered trapezoidal cylinder occurs from the rear corners as well as the top and bottom surfaces of the tapered bluff body [24]. However, in the case of an expanded trapezoidal cylinder, the flow separation occurs only from the rear corners of the bluff body for the range of conditions covered in this work. This accounts for the difference in the Reynolds number range for the onset of flow separation for the expanded and the tapered trapezoidal bluff bodies. Also, the expanded trapezoidal cylinder is a more streamlined body as compared to the other two because the front side of the expanded trapezoidal cylinder has a length which is half of that of the tapered and the square cylinders. This can be emphasized with affirmation because the present work focuses for flow starting from Re = 1 and the Reynolds number range goes up to Re = 150. It was profoundly observed that the flow separation already existed during simulation for Re = 1.

The two wakes formed behind the obstacle (i.e. behind the expanded trapezoidal cylinder) are symmetric along the mid plane in the steady regime for the range Re = 1 – 47 (Fig. 5). As expected, the size of the vortices behind the rear surface of the trapezoidal cylinder increases with the increasing value of the Reynolds number in the steady flow

regime. This nature is found to be similar to that of the flow across a square [15, 16] and a tapered trapezoidal [24] cylinders. Broadly, the wake region for the expanded trapezoidal cylinder is found to lie in between square [28, 57] and tapered trapezoidal [24] cylinders, as can be seen in Fig. 5 for the range of settings covered in the current study. Whereas, with further increasing the value of Re, this behavior is not existent any more and the wakes formed behind the bluff for the range Re = 48 - 150, are no longer symmetric around the central axis.

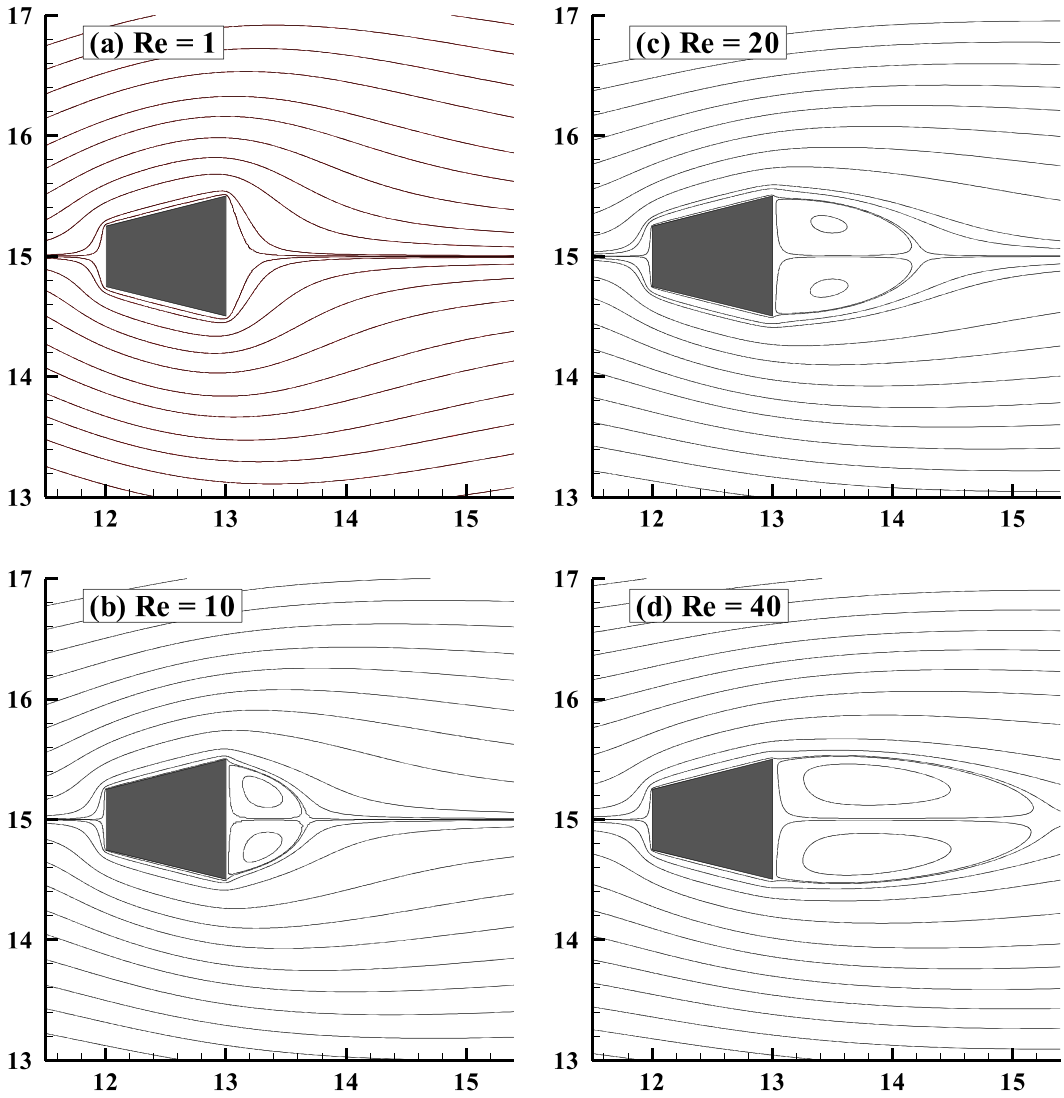

Figure 5: *Streamline contours for Re = 1, 10, 20 and 40 in the steady regime*

While discussing about the transition of flow from steady to unsteady periodic regime it can be vividly stated that it occurs between Re = 47 and 48 for the expanded cylinder. In order to

demarcate between steady and time-periodic regimes, the values of the physical parameters like drag and lift coefficients, and Nusselt number are monitored and plotted with time.

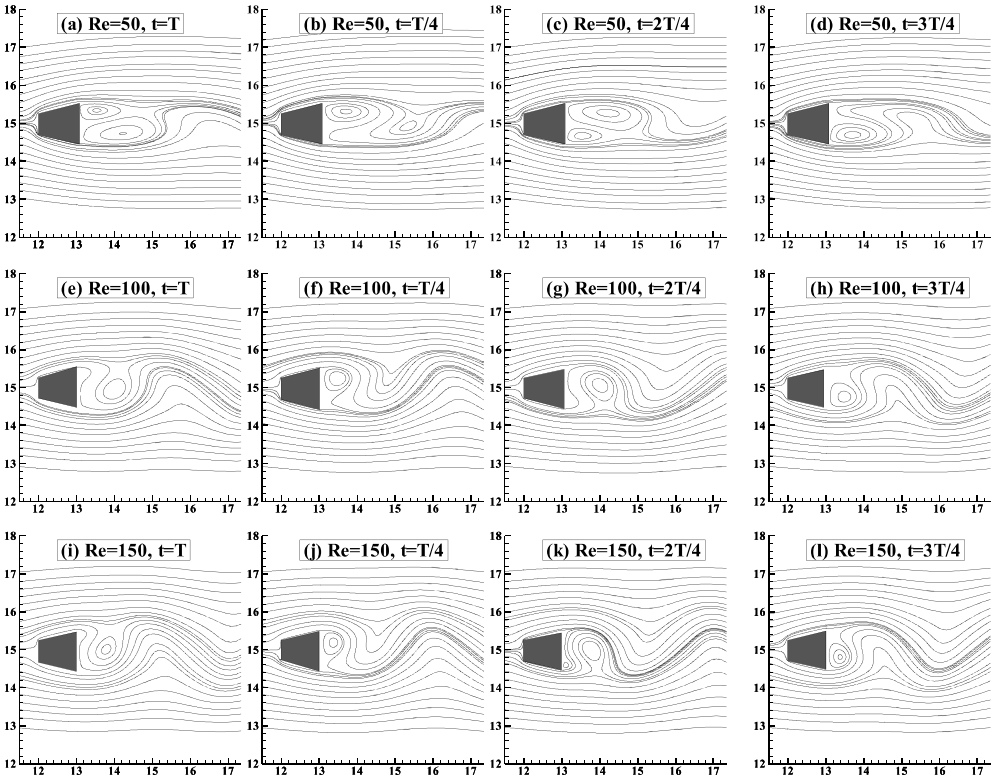

Figure 6: *Instantaneous streamline contours for (a - d) Re = 50, (e - h) 100 and (i - l) 150 in the unsteady regime*

Further, the streamline contours have also been scrutinized to determine the type of flow. Figures 7 (a, b) present the transition from steady to time-dependent regime by streamline contours for Re = 47 and 48, though it depends upon the ratio of front width to rear width of the expanded trapezoidal cylinder. When comparing this transition regime to that for the flow across a tapered trapezoidal cylinder [24], it is observed that it occurs later for the expanded cylinder as it is more streamlined body than that of the tapered one. The transition for the tapered cylinder is found to occur between Re = 46 and 47 [24].

Because the flow is found to be (periodic) unsteady in the range Re = 48 – 150, the instantaneous streamline contours for the Reynolds numbers of 50, 100 and 150 are illustrated in Fig. 6. Here, the instantaneous streamline contours are shown for four successive moments of time (i.e., T, T/4, 2T/4 and 3T/4), which span over the whole time period. It is also observed that from the next moment onwards (i.e., after t = 3T/4), the flow behavior gets repeated. Clearly, similar to a tapered trapezoidal cylinder [24], the vortices in

the separation bubble start to separate alternatively, but at the trailing edge of the expanded cylinder. Similarly, vortices are observed to disappear in the far downstream field for both tapered and expended trapezoidal cylinders.

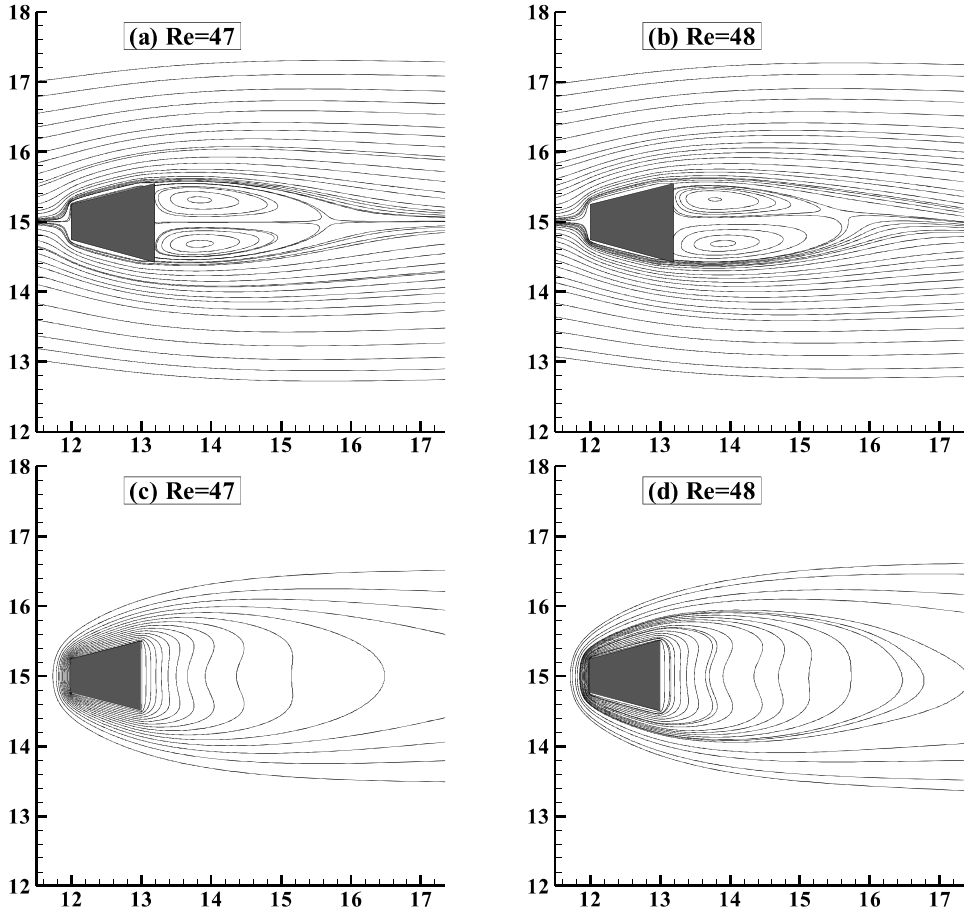

Figure 7: *Temporal variation of (a, b) streamline and (c, d) temperature contours for Re = 47 and 48*

Part 2: Flow patterns are represented by streamline contours, which are a group of constant velocity lines in the domain. Figures 8 - 12 illustrates the streamline contours at different values of Reynolds number (1, 5, 10, 20 and 40) and power-law index (0.4 - 1.8). It can be observed from these figures that for shear-thinning liquids (n < 1), the flow is attached to the surface of the long trapezoidal obstacle at Reynolds number (Re) for any value of power-law index (n) (Figs. 8 and 9). In other words, there is no separation of flow from the tapered cylinder because of the dominance of viscous forces at low Reynolds numbers ($\mathrm{Re} \leq 5$). The flow; however, begins to separate from the trailing edge of the cylinder at Re =

10 for n = 0.6 (Fig. 10).

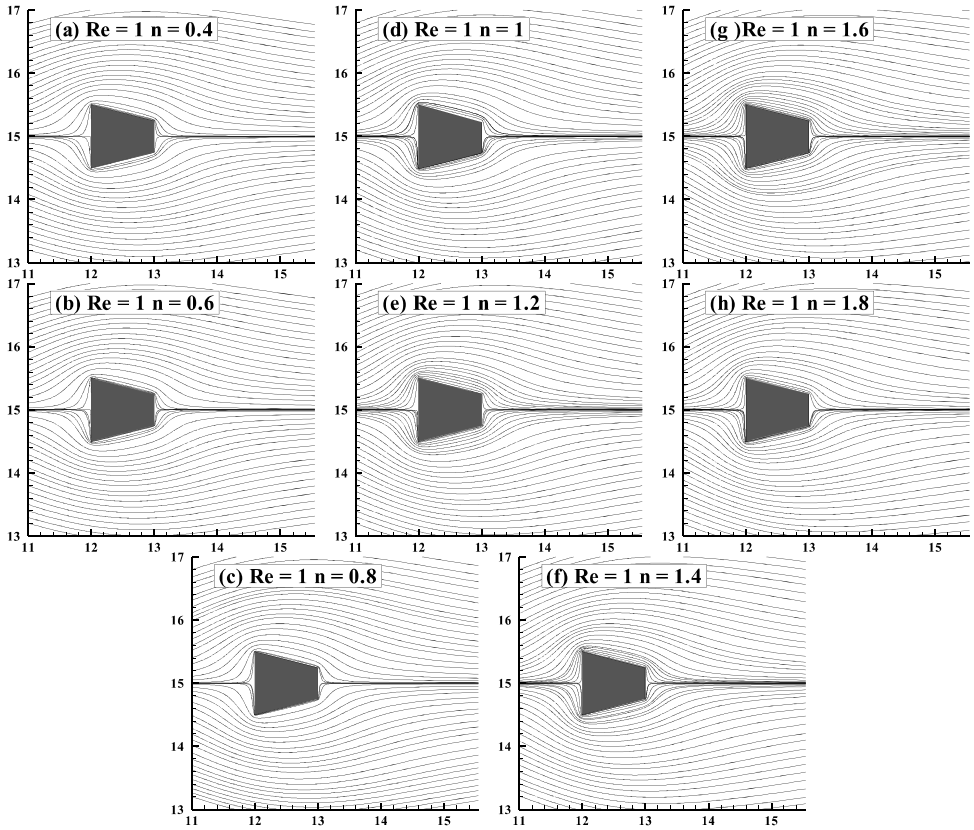

Figure 8: *Streamline contours for power-law index (n) = 0.4 - 1.8 for shear-thinning (a - c), Newtonian (d) and shear-thickening (e - h) fluids for Re = 1*

For the power-law index of unity (i.e., Newtonian case) the onset of flow separation is reported to occur between Re = 5 and 6 for a tapered trapezoidal obstacle in the unconfined domain [24] (Figs. 8 - 10). Along the same line, for another similar bluff body, i.e., a long square cylinder, the onset of flow separation exists between Re = 1 and 2 [28, 57]. For the case of shear-thickening liquids (n > 1), it can be noticed that at Re = 1 and $1 < n < 1.6$ the flow is un-separated from a long tapered trapezoidal bar (Fig. 8). However, with gradually increasing power-law index ($n \geq 1.6$), the flow separates and vortices develop downstream of a cylinder (Fig. 8). Therefore, it can be stated from Figs. 8 - 12 that with the increase in the value of power-law index for a fixed value of Reynolds number inception of flow separation occurs early.

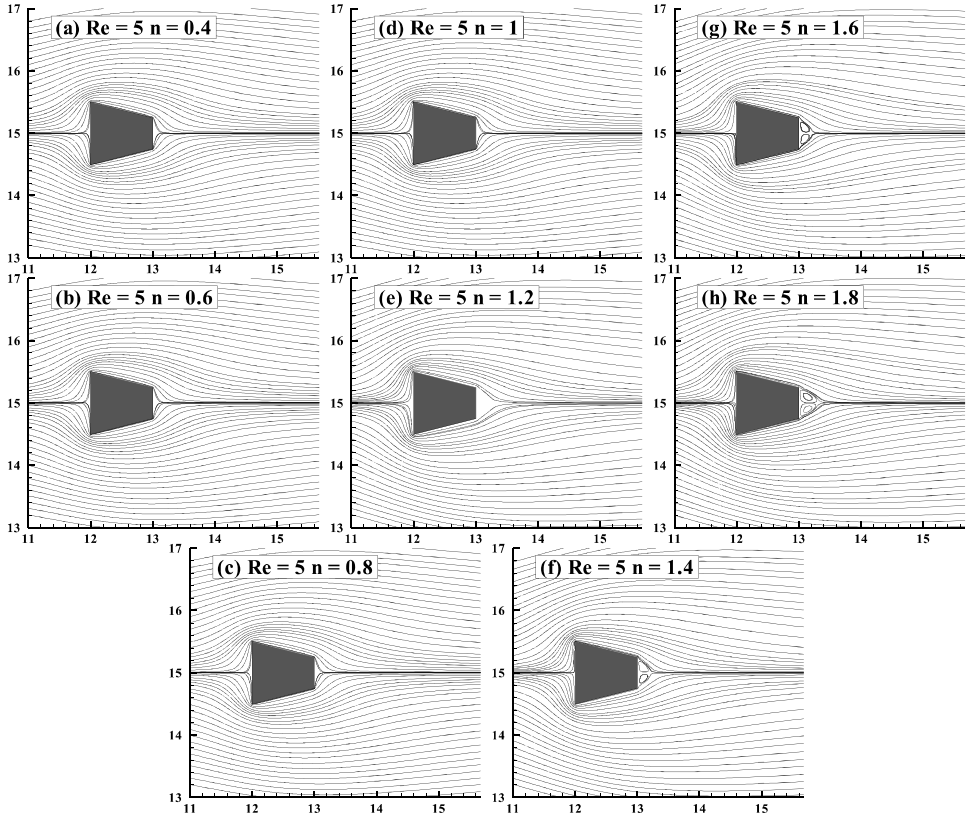

Figure 9: *Streamline contours for power-law index (n) = 0.4 - 1.8 for shear-thinning (a - c), Newtonian (d) and shear-thickening (e - h) fluids for Re = 5*

As soon as the flow starts to separate from the obstacle, it leads to the formation of two standing wakes downstream of a tapered cylinder. Similar to a long square bluff body [28, 57], as the value of the Reynolds number increases the size of symmetric vortices also increases. Furthermore, with the increasing value of the power-law index for a constant value of Reynolds number, the wake region increases in size. Eventually, it can be found for shear-thickening liquids (n > 1), the time-periodic behaviour starts at Re = 40 for $n > 1.4$.

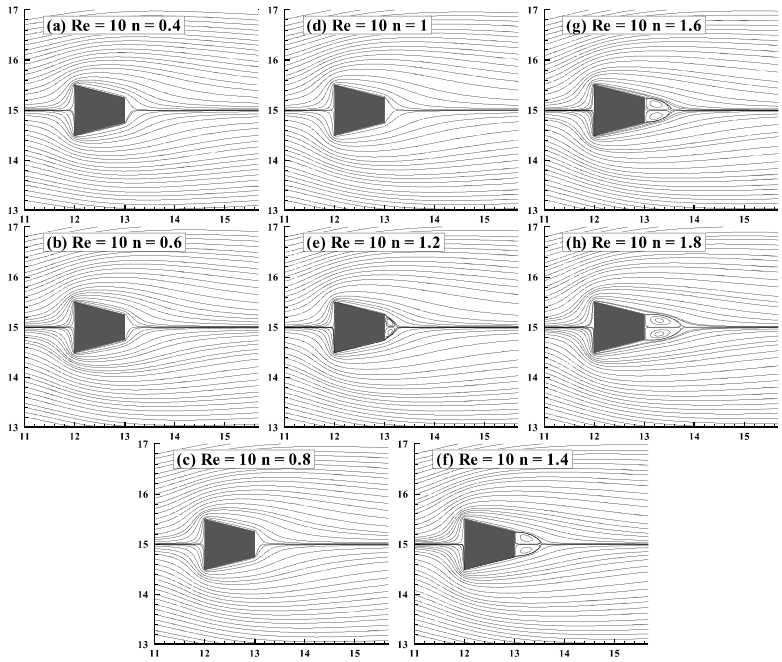

Figure 10: *Streamline contours for power-law index (n) = 0.4 - 1.8 for shear-thinning (a - c), Newtonian (d) and shear-thickening (e - h) fluids for Re = 10*

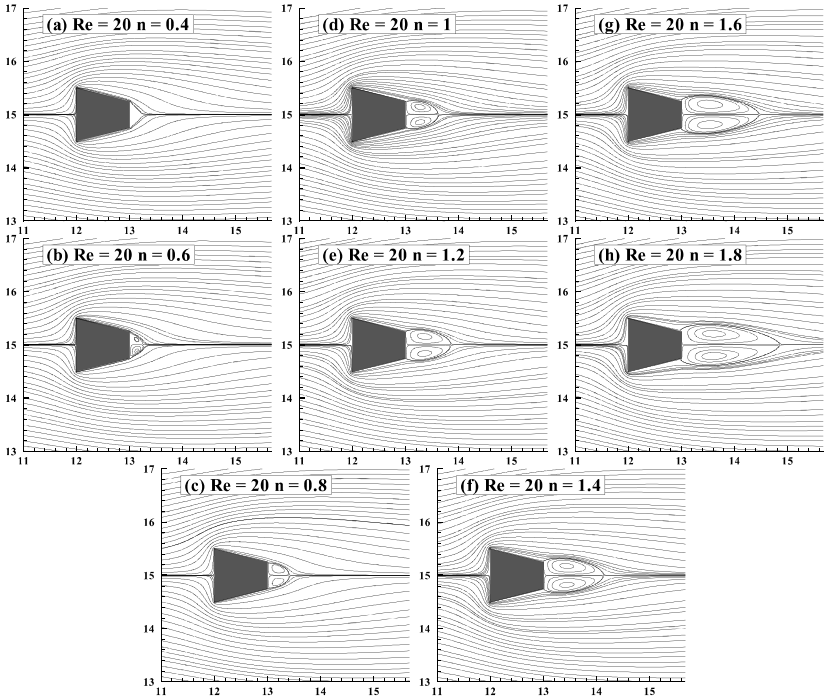

Figure 11: *Streamline contours for power-law index (n) = 0.4 - 1.8 for shear-thinning (a - c), Newtonian (d) and shear-thickening (e - h) fluids for Re = 20*

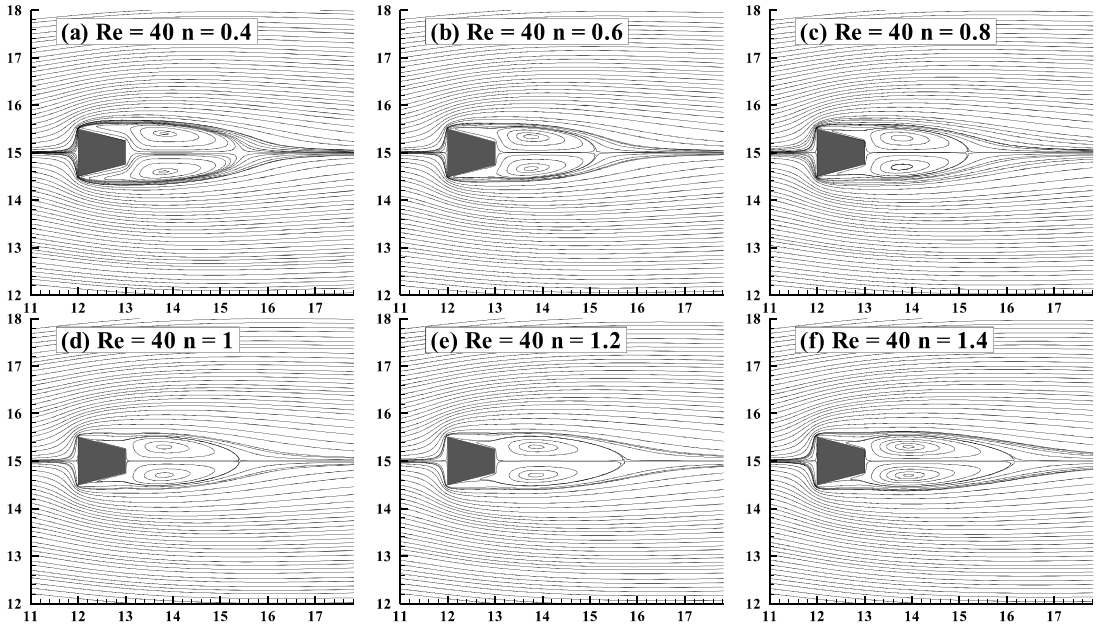

Figure 12: *Streamline contours for power-law index (n) = 0.4 - 1.4 for shear-thinning (a - c), Newtonian (d) and shear-thickening (e - h) fluids for Re = 40*

4.3 Thermal patterns

Part 1: The effects of Reynolds number on thermal structures around an expanded trapezoidal bluff body are investigated for Re = 1 – 150 in both steady and unsteady regimes at Pr = 0.7. Figures 13 (a-d) present the isotherm contours in the steady regime for Re = 1, 10, 20 and 40. Obviously, the thermal effects are observed to be more prominent at the low values of Reynolds number as viscous forces are more dominant in the steady regime. As the value of Reynolds number is increased gradually, it is observed that temperature fields decay in the steady flow regime with the increasing Re. Because the flow field is steady for the range, the symmetry in the temperature field about the mid plane can be seen in Figs. 7c and 13. For the range of Reynolds number of in the steady flow regime, isotherms are observed to be turning towards the rear surface of the expanded trapezoidal cylinder. This nature again finds suitable agreement with the isotherms of a tapered trapeze as well, where the turning occurs in the range of Reynolds number of in the steady regime. It clearly highlights the effects of geometry and shape on the heat transfer rate.

The instantaneous isotherm contours for four successive moments of time for the time-dependent regime, which span over the whole period are presented at different values of Reynolds numbers for the air as working fluid in Fig. 14.

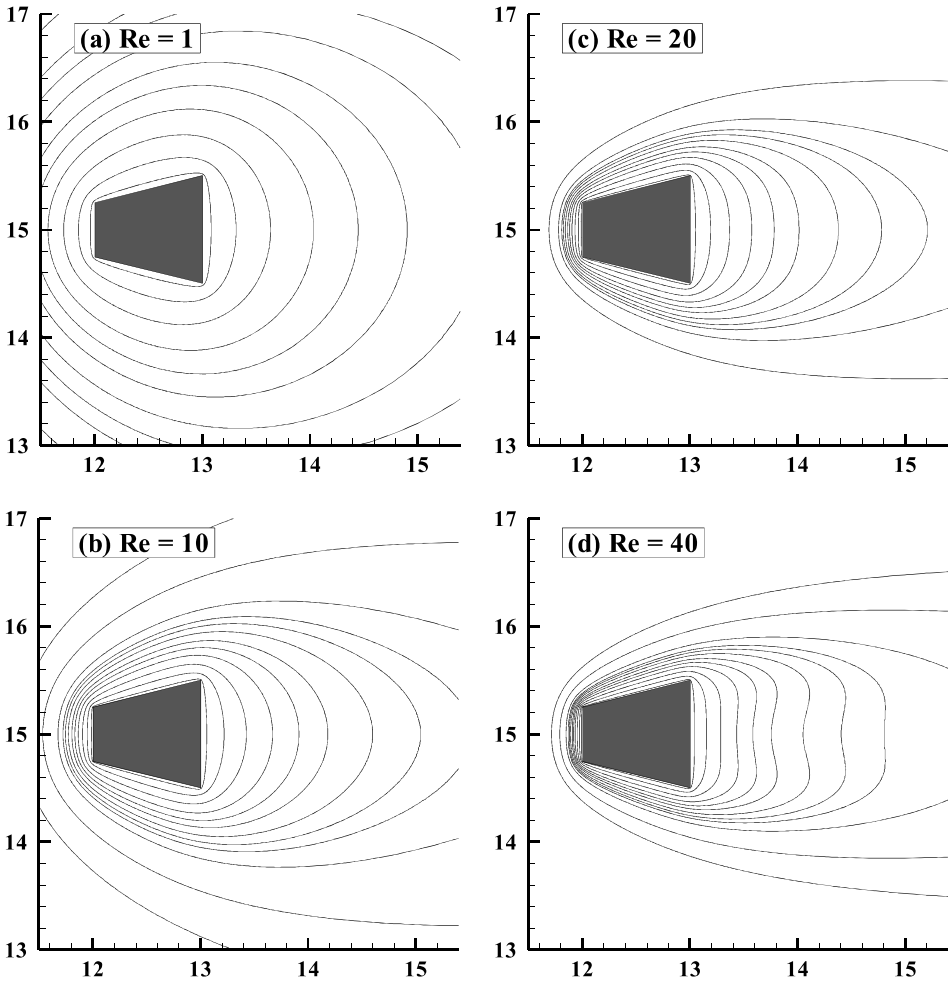

Figure 13: *Isotherm patterns in the steady regime (Re=1, 10, 20 and 40)*

Similar to the instantaneous flow profiles, the isotherms also seem to possess the nature of alternating reversals and the temperature street behind the cylinder is formed. It can be seen from these figures that the wavering motion of isotherms increases with the increasing value of the Reynolds number. Also, the disturbance on the larger base width of the trapezoidal cylinder increases with the increasing value of the Reynolds number.

Similar to a square [28, 57] and a tapered trapezoidal [24] cylinders, the maximum crowding of isotherms is observed on the front surface of the expanded trapezoidal bluff body. This is quite evident from the thermal patterns in Fig. 14, thereby resulting in higher heat transfer from the front surface of the expanded trapezoidal cylinder as compared to other surfaces of the expanded cylinder.

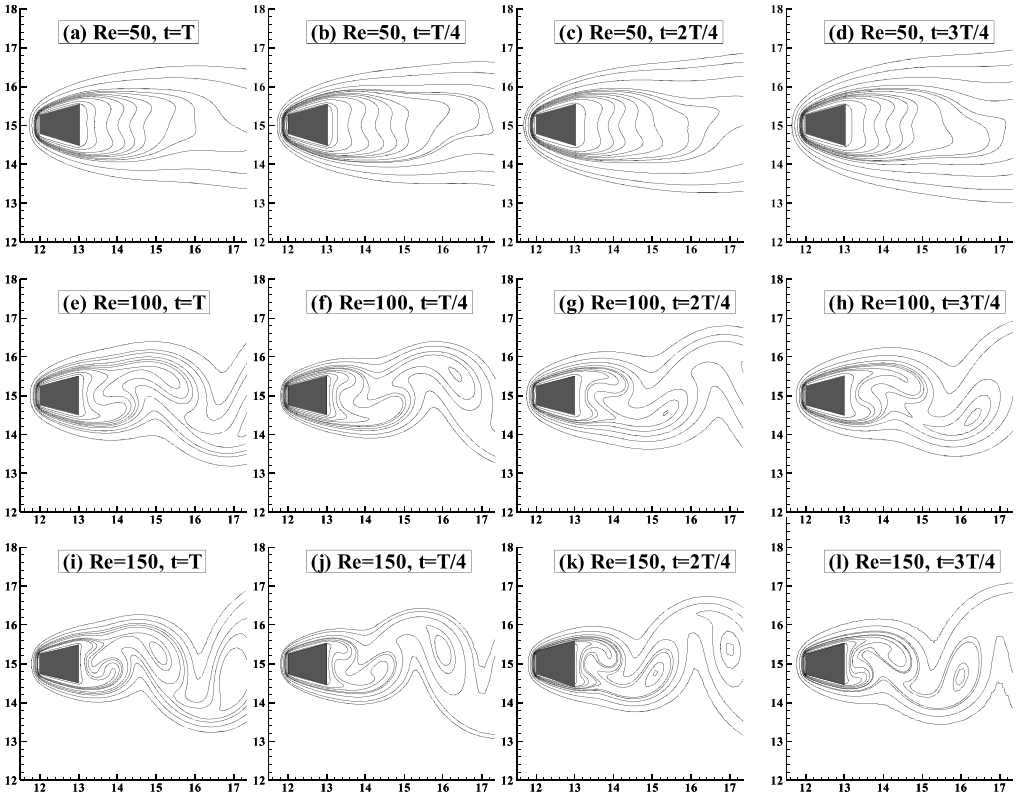

Figure 14: *Isotherm profiles for (a - d) Re = 50, (e - h) 100 and (i - l) 150 in the unsteady regime*

Part 2: Isotherm contours for Re =1, 5, 10, 20 and 40 in the steady regime are shown in Figs. 15 - 19 respectively for n = 0.4 - 1.8 and Pr = 50. It is also needed to be highlighted here that numerous petroleum products and ethylene glycol-water mixtures have Prandtl numbers up to ~ 50 or so [33 - 35]. Further, as the heat transfer from the cylinders is guided by the flow, the isotherm patterns can be classified in the same way as the streamline patterns mentioned in the previous section. The symmetry in the temperature field about the mid-point can be observed as the flow is steady for Re < 40 (n = 0.4 – 1.8) (Figs. 15 - 18) and for Re = 40 (n = 0.4 – 1.4) (Fig. 19). The flow becomes time-periodic at Re = 40 for n> 1.4. As expected, for shear-thinning, Newtonian and shear-thickening behaviors ($0.4 \le n \le 1.8$), it can be found that with increase in Reynolds number the temperature field decays. On the other hand, with the increasing value of power-law index, the temperature field becomes more intensified.

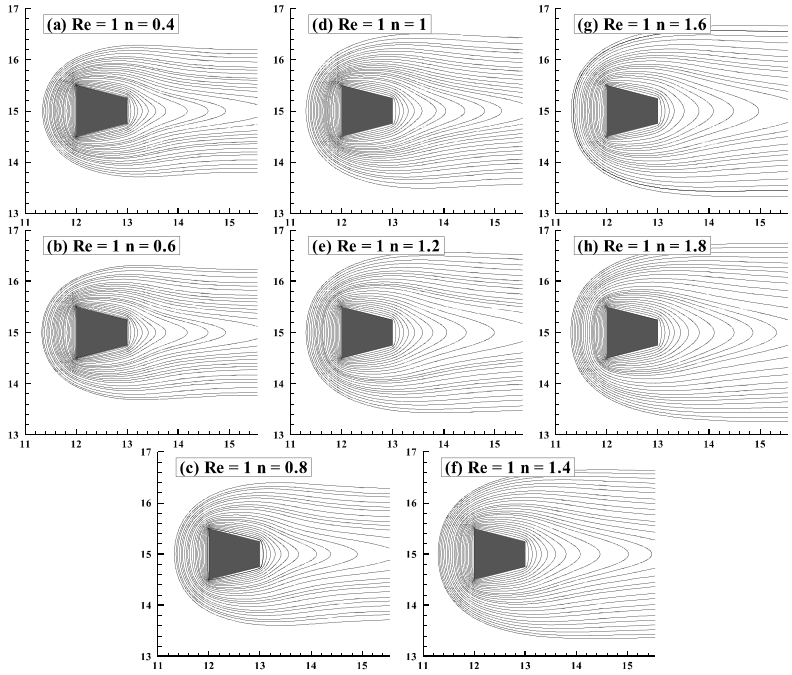

Figure 15: *Isotherm contours for power-law index (n) = 0.4 - 1.8 for shear-thinning (a - c), Newtonian (d) and shear-thickening (e - h) fluids for Re = 1*

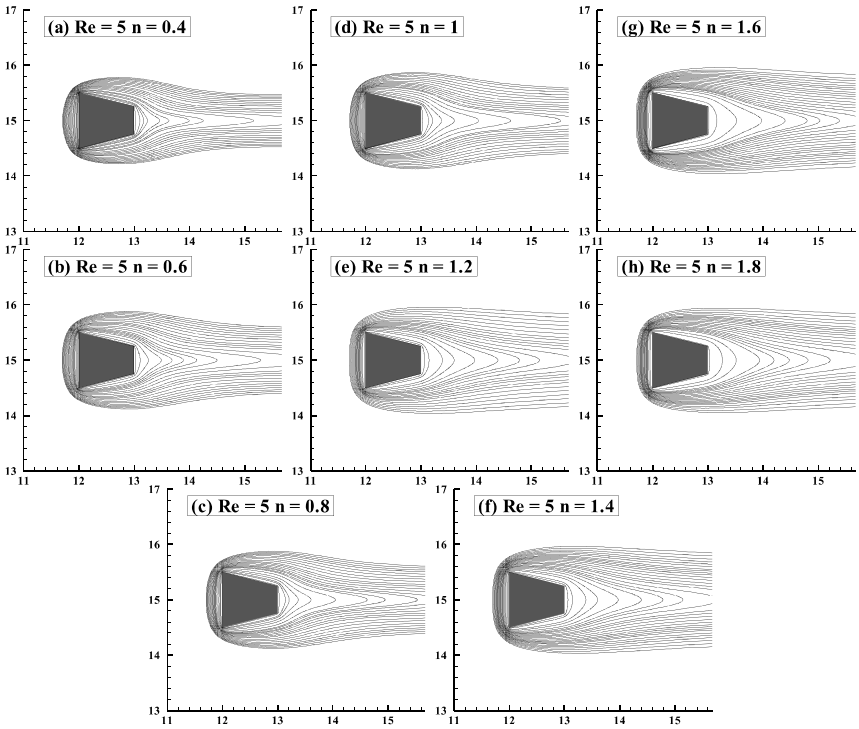

Figure 16:*Isotherm contours for power-law index (n) = 0.4 - 1.8 for shear-thinning (a - c), Newtonian (d) and shear-thickening (e - h) fluids for Re = 5*

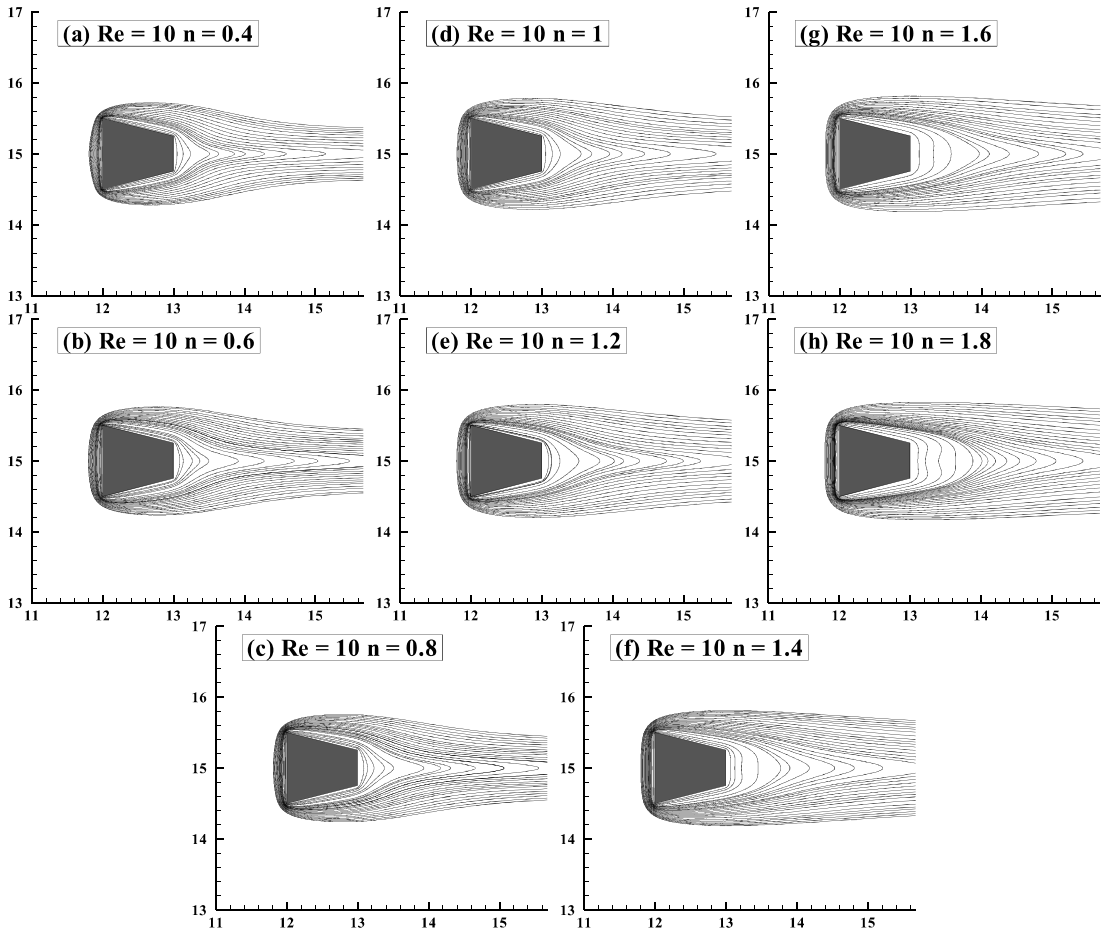

Figure 17: *Isotherm contours for power-law index (n) = 0.4 - 1.8 for shear-thinning (a - c), Newtonian (d) and shear-thickening (e - h) fluids for Re = 10*

It can also be seen that at low Reynolds number the isotherms are more prominent as conduction is intensified, e.g., at the value of the Reynolds number of unity.

The isotherms are observed to be turning towards the rear surface of a tapered trapezoidal cylinder for the range of Reynolds number $20 \leq \mathrm{Re} \leq 40$ at Pr = 50 and n = 1 in the steady regime (Fig. 18). For shear-thinning fluids (n< 1), the turning of isotherms is observed at Re = 40 and n = 0.4 (Fig. 19). However, for shear-thickening fluids (n> 1), the turning in isotherms is seen to initiate at Re = 10 for n = 1.4 (Fig. 17); thereby throwing light on the fact that with the increasing value of power-law index, the inception of turning of isotherms occurs early.

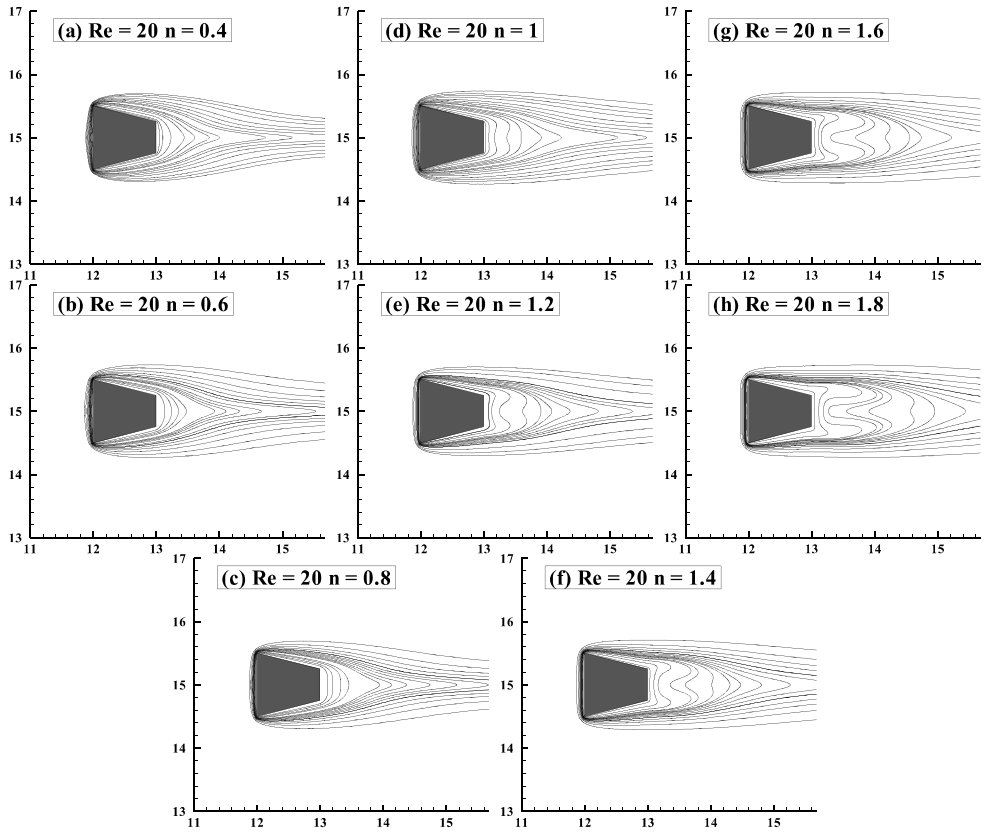

Figure 18: *Isotherm contours for power-law index (n) = 0.4 - 1.8 for shear-thinning (a - c), Newtonian (d) and shear-thickening (e - h) fluids for Re = 20*

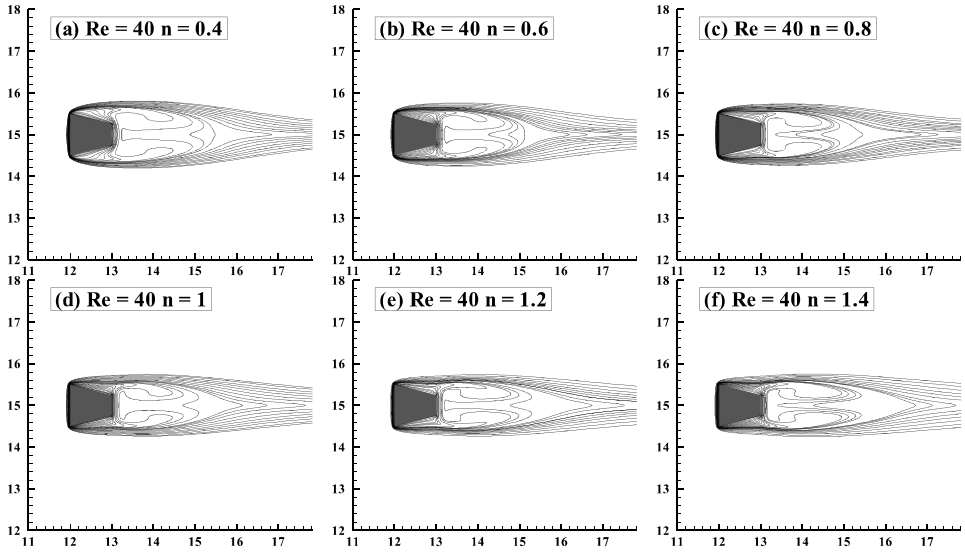

Figure 19: *Isotherm contours for power-law index (n) = 0.4 - 1.4 for shear-thinning (a - c), Newtonian (d) and shear-thickening (e - h) fluids for Re = 40*

4.4 Wake Length

Part 1: Figure 20 shows the variation of the wake or recirculation length for the expanded cylinder with Reynolds number in the steady regime along with the literature values for the tapered [24] and the square [57] cylinders. The wake length is the length of the closed near wake and it is measured from the rear surface of each cylinder considered here. Similar to a square cylinder [57], the recirculation length for an expanded cylinder increases linearly with the increase in Reynolds number. The wake length is slightly higher for the expanded cylinder than that of the square cylinder up to Re = 10; however, for Re > 10, an opposite trend of the wake length is observed with the increasing difference in the values of wake lengths for the two obstacles. Figure 20 contains the values of the wake length for $2 \leq \mathrm{Re} \leq 45$ as the onset of flow separation for the square cylinder is reported in between Re = 1 and 2, and the transition to unsteady exists after Re = 45 [57]. When a comparison is made between the recirculation length formed behind the expanded trapezoidal cylinder and that behind the tapered trapezoidal bluff body [24] for different values of Reynolds number, it has been observed that the recirculation region did not even exist for $\mathrm{Re} \leq 5$, for the case of tapered trapeze which is in contrast to that of the expanded cylinder, where the wake region exists at those corresponding values of Re. The main reason behind this is that the onset of flow separation exists for Re < 1 in case of the expanded cylinder; whereas, it occurs at the Reynolds number range of $5 \leq \mathrm{Re} \leq 6$ for the tapered counterpart [24]. Further, it is observed that the size of the wake for the expanded cylinder is bigger than the tapered one for the range of Reynolds number $1 \leq \mathrm{Re} \leq 30$. However, for Re = 40, it has been found that the wake length is higher for the tapered trapeze. This anomaly is due to the fact that the separation of flow in the case of tapered trapezoidal cylinder takes place from top and bottom surfaces along with the rear corners. However, in the present case of an expanded cylinder, flow separation occurs only from the rear corners because of its streamline shape for the range of settings covered.

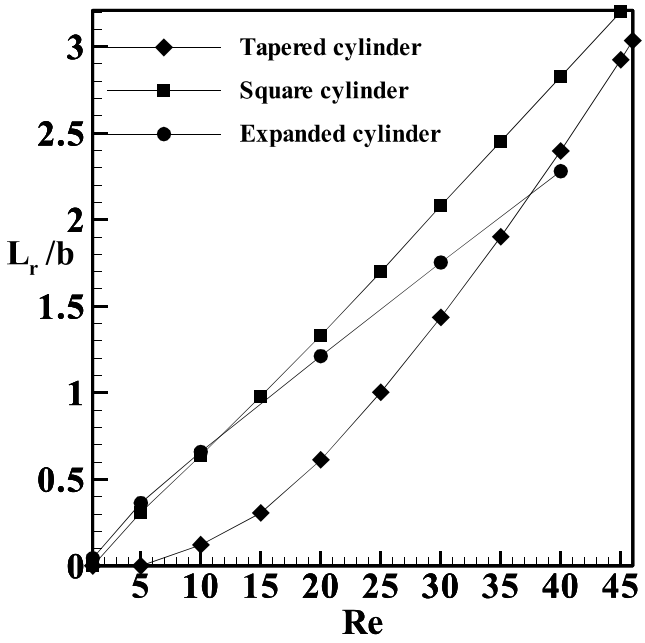

Figure 20:*Variation of the wake length along with the values of tapered trapezoidal cylinder [24] and of square cylinder [57] in the steady regime*

Furthermore, as the variation of wake length (L_r / b) with Reynolds number (Re) in the steady flow region is found to be linear, the following empirical equation is correlated for the intermediate values of the physical parameters.

$$L_r / b = 0.086\,\mathrm{Re}^{0.883} \tag{12}$$

When the maximum deviation from the present computed results with the values obtained from equation (12) is calculated, it has been recorded to be as low as 1.99% for Re = 5, 0.67% for Re = 20 and 2.04% for Re = 40.

Part 2: The wake length or recirculation length is determined here as the distance from the rear surface of the obstacle to the point of attachment for the near closed streamline on the axis of symmetry. The wake length is found to be zero for the range of settings: Re = 1 ($n < 1.6$), $\mathrm{Re} = 5$ ($n < 1.2$) and $\mathrm{Re} = 10$ ($n < 0.6$). It can be seen that with increase in Re, the wake length increases for a constant value of *n*. Broadly speaking, with increase in power-law index from 0.4 to 1.8, the wake length increases with Re. However, this trend is not obeyed at *n* = 0.4. The primary reason behind this is undoubtedly due to the highly non-linear nature of the governing equations for the high shear-thinning fluids. As expected, the wake length for

Newtonian liquids lie mid-way between shear-thinning and shear-thickening liquids, and the shear-thickening liquids possess the highest value of the wake length.

4.5 Individual and overall drag coefficients

Part 1: Steady and unsteady flow past any obstacle can also be quantified by visualizing the behavior of the drag. The overall drag coefficient around any bluff body is calculated as $C_D = C_{DF} + C_{DP}$. The variation of individual (C_{DF}, C_{DP}) and overall (C_D) values of the drag coefficients with varying values of the Reynolds number is shown in Figs. 10 (a - c). The variation of individual and total drag coefficients for the square cylinder [28, 57] and the tapered trapezoidal cylinder [24] can also be seen in these figures. A magnified view of Fig. 10c is also presented on the top right corner to illustrate the comparison more extensively**.**

The values of friction and pressure drag coefficients decrease with the increasing value of the Reynolds number for all three sharp edged bluff bodies (viz. expanded, tapered and square cylinders) considered in the steady flow regime (Fig. 21a, b). The friction drag coefficient (Fig. 21a) for the expanded trapezoidal cylinder at different values of Reynolds number is found to have higher values than that of the friction drag coefficient for the tapered and the square cylinders in the steady regime. The values of friction drag acting on a square cylinder exist between that of the expanded and the tapered trapezoidal cylinders. On the other hand, the pressure drag of the expanded cylinder (Fig. 22b) is observed to be lower than that of the square and the tapered trapezoidal cylinders. However, the pressure drag of the tapered cylinder (Fig. 21b) is observed to be higher for the range $\mathrm{Re} \geq 10$ and lower for the range $\mathrm{Re} < 10$ as compared to the square cylinder in the steady regime [57].

Similar to a tapered cylinder [24], Fig. 21(c) throws light on the fact that as we increase the value of the Reynolds number for the case of an expanded cylinder, the value of the total drag coefficient decreases up to a certain Reynolds number and thereafter it increases with the increasing Reynolds number. The minimum drag coefficient is found here at the Reynolds number of 90; however, in the case of a tapered one [24], the minimum value of the drag is reported at Re = 50. This is due to the streamline shape of the expanded trapezoidal cylinder. The overall drag coefficient for the expanded trapezoidal cylinder is found to be lower than the square cylinder [28, 57] and the tapered trapezoidal cylinder [24] for the range of settings studied**.** While the overall drag coefficient for the tapered trapezoidal

cylinder [24] is found to be lower for the range $1 \le \mathrm{Re} \le 50$ and higher for the range $50 < \mathrm{Re} \le 150$ than the square cylinder [28, 57].

To correlate the present values of the drag coefficient for the expanded cylinder at different values of the Reynolds numbers in the steady flow regime ($1 \le \mathrm{Re} \le 47$), an empirical equation (13) has been found adequate.

$$C_D = 0.6142 + 11.6502\ \mathrm{Re}^{-0.6921} \tag{13}$$

While comparing the above correlation with the present computed data, it has been observed that the maximum deviation in the drag coefficient is about 1.81% for the Reynolds number of unity. The corresponding maximum deviation reduces to the value of about 0.74% at Re = 40. Further, the maximum deviation is only around 0.37% at Re = 47, after which transition starts occurring from steady to unsteady regime.

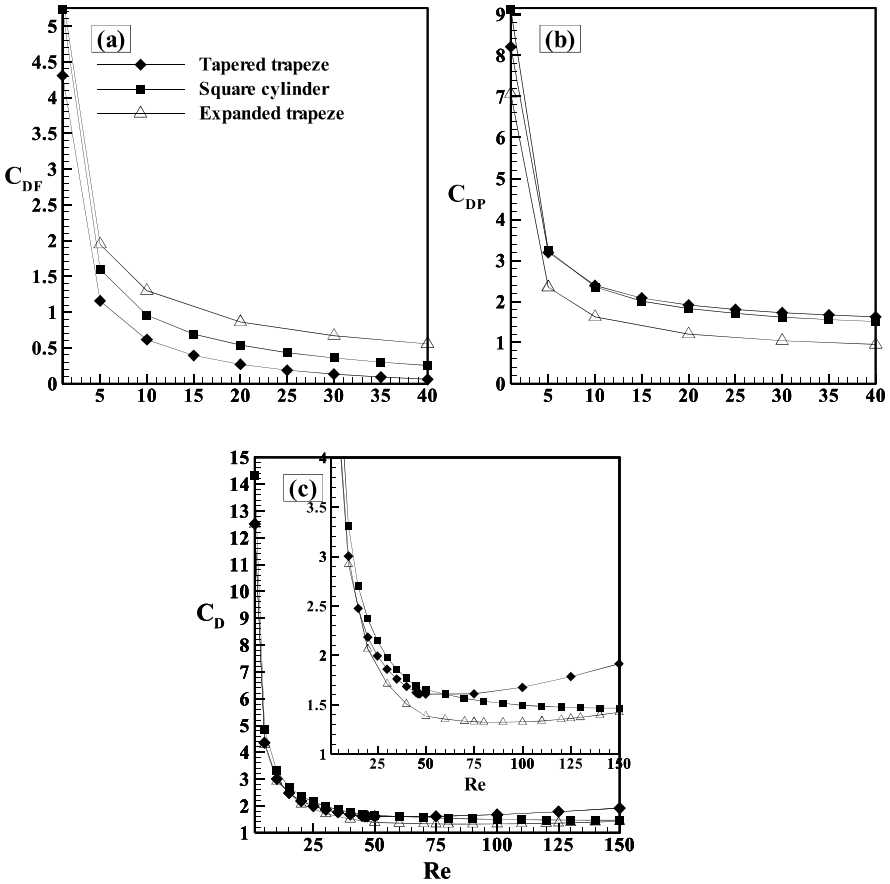

Figure 21: *Variation of (a, b) individual and (c) overall drag coefficients along with the results of square cylinder [57] and tapered trapezoidal cylinder [24] with Reynolds number*

Part 2: The drag force exerted on a long tapered trapezoidal bar is consisting of two components, namely, viscous drag and pressure drag. The total drag coefficient (C_D) is a measure of this drag force and it is defined as follows:

$$C_D = \frac{2F_D}{\rho U_\infty^2 b} = C_{Dp} + C_{Df} \tag{14}$$

where,

$$C_{Dp} = \frac{2F_{Dp}}{\rho U_\infty^2 b} = \int_S C_p n_x dS \text{ and } C_{Df} = \frac{2F_{Df}}{\rho U_\infty^2 b} = \frac{2}{\mathrm{Re}} \int_S (\tau . n_s) dS$$

It can be observed that individual and total drag coefficients vary inversely and non-linearly with Reynolds number for a fixed value of power-law index. It can be stated that the contribution of pressure drag is always more than that of friction drag to the overall drag for the ranges of Reynolds numbers considered in the steady regime. The friction drag coefficient decreases with an increase in power-law index for a fixed Reynolds number till a certain value of Re; whereas, a reciprocal effect is observed for higher Re. The total drag coefficient increases with an increase in power-law index till a certain value of Re and then decreases.

4.6 Temporal drag and lift coefficients, and Nusselt number

The variation of the time history of drag coefficient, lift coefficient and Nusselt number for the case of flow and heat transfer across an expanded trapezoidal bluff body is shown in Fig. 22. In this study, computational fluid dynamic analysis is carried out until 10 cycles of almost constant amplitude are obtained for drag and lift coefficients, and Nusselt number with time. The frequency of the lift coefficient is found to be twice of that of the drag coefficient, which is consistent with Chen et al. [26]. Similarly, the frequency of the lift coefficient is found to be twice of that of the Nusselt number. Furthermore, the instantaneous values of drag, lift and Nusselt number in 10 cycles of constant amplitudes are utilized to calculate their time-averaged values.

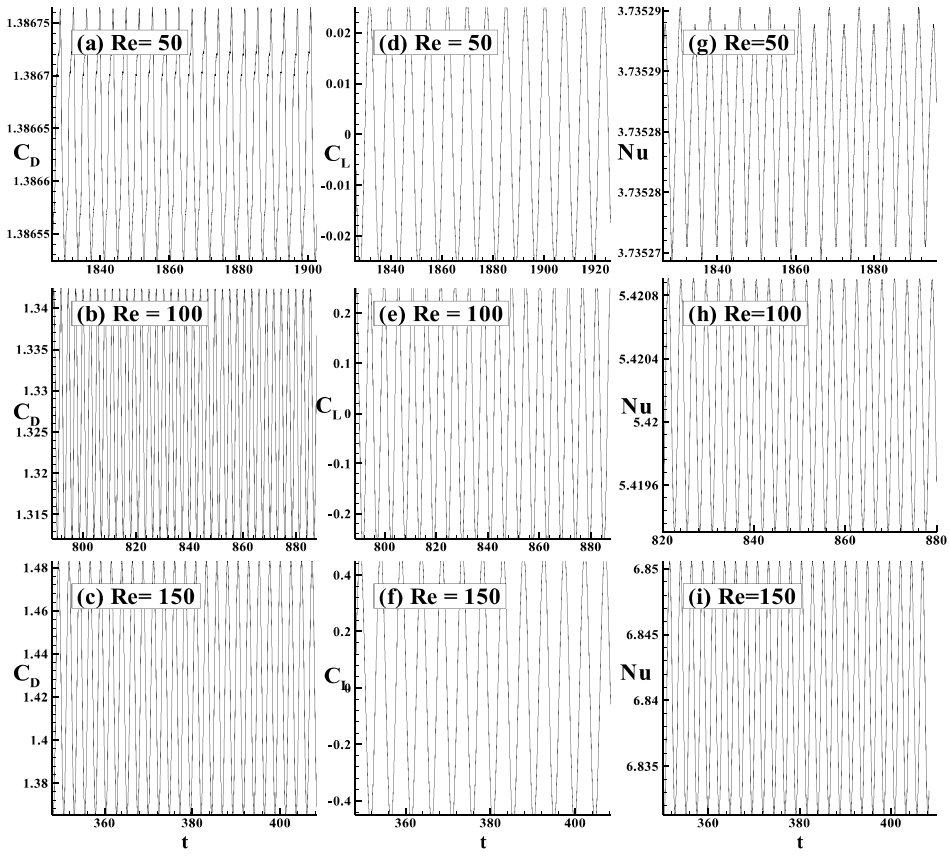

Figure 22: *Time history of (a-c) drag, (d-f) lift and (g-i) Nusselt number at at Re= 50, 100 and 150 in the unsteady periodic regime*

The time-averaged values of any quantity (φ) can be calculated by using the following relationship

$$\varphi_{mean} = \frac{\sum_{i=1}^{N} \varphi_i}{N} \tag{14}$$

where N is the total number of time steps in 10 cycles.

4.7 Strouhal number

It is well known that the non-dimensional frequency of oscillation in lift is termed as Strouhal number ($St = fb/U_\infty$), and the frequency of vortex shedding f is measured from the temporal variation of the lift coefficient. The variation of the Strouhal number with Reynolds number in the time-dependent regime for the case of flow and heat transfer across an expanded trapezoidal bluff body is shown in Fig. 23(c) along with the values of tapered [24]

and square [57] cylinders. The Strouhal number is observed to increase with the increasing Reynolds number for the three bluff bodies studied in this work. A detailed analysis of the values of Strouhal number indicates that these values are higher for the expanded trapezoidal cylinder than that of the tapered counterpart [24] and the square cylinder [57], for any comparable value of Reynolds number. Similar to friction drag, Strouhal number for a square cylinder exists between the expanded and the tapered trapezoidal cylinders.

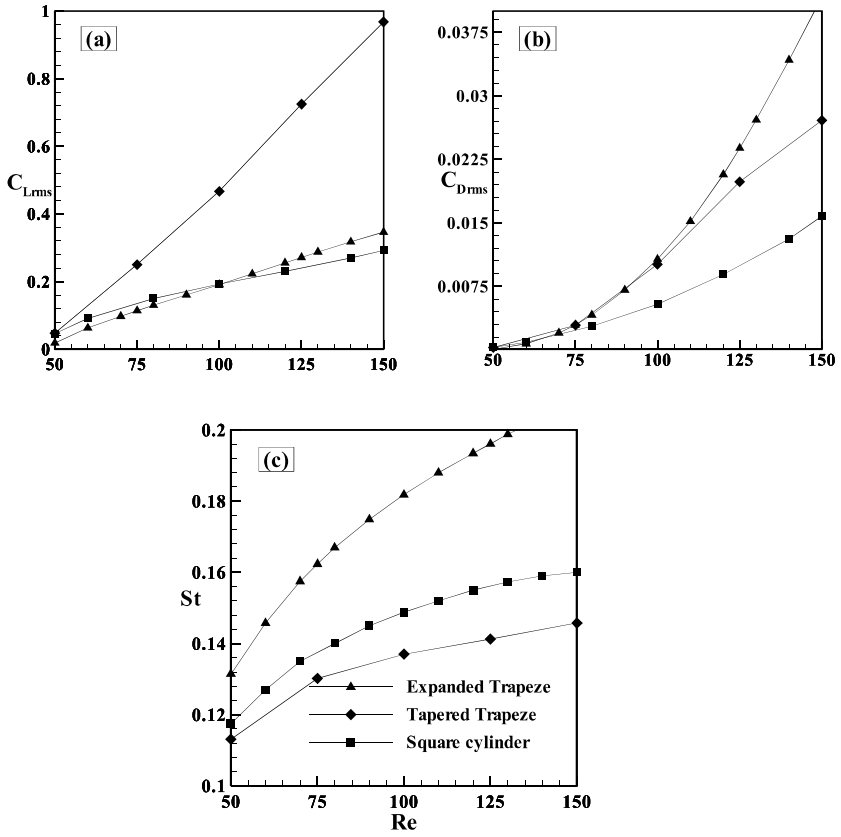

Figure 23: *Variation of (a) the RMS value of the lift coefficient, (b) the RMS value of the drag coefficient and (c) the Strouhal number along with the values of tapered trapezoidal cylinder [24] and square cylinder [57] with Reynolds number*

Also, the difference in the values of Strouhal number for expanded, tapered and square cylinders increases with the increasing Reynolds number. Furthermore, a correlative relationship between the Strouhal number (*St*) and the Reynolds number (Re) for the unsteady (periodic) regime ($48 \le \mathrm{Re} \le 150$) is observed as:

$$St = 0.0127 + 0.026\,\mathrm{Re}^{0.4012} \tag{15}$$

The values obtained from the above empirical correlation (15) showed the maximum deviation of about 1.60% at Re = 75 with the present computed results, which further diminished to a very low value of only about 0.34% for Re = 150.

4.8 Local and average Nusselt numbers

Part 1: The variation in the value of the local Nusselt number (Nu) around the surfaces of the 2-D expanded trapezoidal cylinder for the values of Reynolds numbers of 1, 20 and 40 in the steady regime is illustrated in Figs. 24a – c for the air as the working fluid. On the other hand, instantaneous variation of the local Nusselt number for the four successive moments of time (T, T/4, 2T/4 and 3T/4), which span over the entire period, for Reynolds numbers of 50, 100 and 150 in the time-dependent regime has been shown in Figs. 24d - f. Similar to a square [28, 57] and a tapered [24] cylinders, the value of the local Nusselt number decreases on top (from B to C) and bottom (from A to D) surfaces and then increases sharply towards the rear corners C and D, respectively. On front and rear surfaces of the expanded cylinder, there exists a local minimum in the value of the local Nusselt number near the middle of these surfaces. Clearly, the value of the local Nusselt number affects more on the rear surface with time as compared to top and bottom surfaces of the cylinder in the unsteady regime due to vortex shedding (Figs. 24d - f); however, the front surface remains unaffected with time. However, when compared to these effects, the changes in the value of the local Nusselt number are observed to be more prominent with the increasing value of the Reynolds number. Overall, the variation of the local Nusselt number around the cylinder surfaces is found to be symmetric for top and bottom halves of the expanded cylinder in the steady regime. It has also been observed that the local Nusselt number increases with the increasing Reynolds number.

Figures 25a and b describe the variation of the average Nusselt number ($\bar{N}u$) for an expanded trapezoidal bluff body with Reynolds number in steady and unsteady regimes, respectively. Similar to a square [28, 57] and a tapered [24] cylinders, the value of the average Nusselt number for the expanded cylinder increases monotonically with the increasing value of the Reynolds number in both steady and time-dependent regimes. Further, when the value of the average Nusselt number for an expanded trapezoidal cylinder is compared to that of a square cylinder [28, 57], it is found that the value of the average Nusselt number for the former shows higher value than the latter for the entire range of Reynolds number of 1 to 150. Similarly, the average Nusselt number for an expanded

trapezoidal cylinder is always higher than that for the tapered one [24]. The effect of streamline shape of the expanded cylinder accounts for this increase in the value of the average Nusselt number. If compared with the square cylinder [28, 57], the average Nusselt number for the trapezoidal cylinder is found to be higher for $\mathrm{Re} < 10$ and lower for $10 \le \mathrm{Re} \le 150$. The augmentation in heat transfer is also calculated at different values of Reynolds number and is given in Table 3. The maximum percentage enhancement in heat transfer for the expanded trapezoidal cylinder with respect to the tapered trapezoidal cylinder [24] and the square cylinder [28, 57] are found to be approximately 146% and 141%, respectively at Re = 150.

Table 3: *Percentage (%) enhancement in heat transfer for the expanded trapezoidal cylinder with respect to (w.r.t.) the tapered cylinder [24] and the square one [28, 57]*

Re	Nu			% Enhancement w.r.t. tapered cylinder	% Enhancement w.r.t. square cylinder
	Expanded cylinder	Tapered cylinder	Square cylinder		
1	0.7885	0.7372	0.7033	107	112
20	2.4858	1.9876	2.0569	125	121
40	3.3693	2.5110	2.6969	134	125
50	3.7353	2.7212	2.9805	137	125
100	5.4201	3.7974	4.0440	143	134
150	6.8408	4.6787	4.8388	146	141

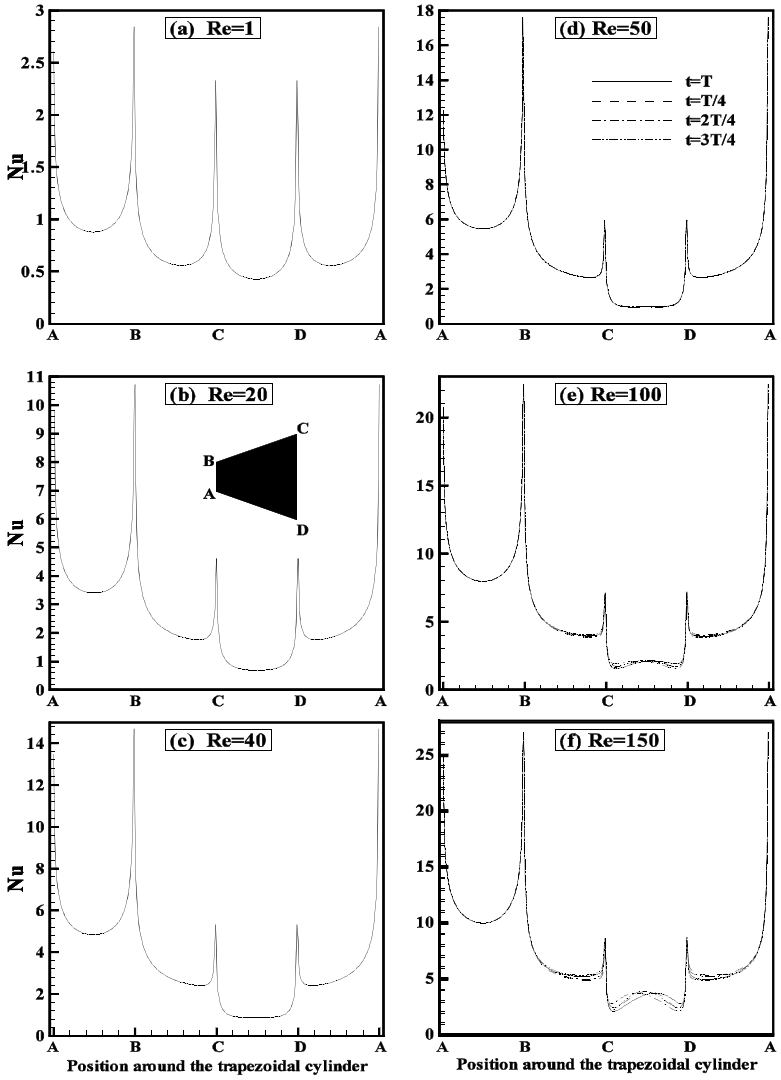

Figure 24: *Variation of the local Nusselt number around the surfaces of the expanded trapezoidal cylinder for Re = 1, 20, 40, 50, 100 and 150 at Pr=0.7*

Furthermore, an empirical correlation has been derived (equation 16) to obtain the value of the average Nusselt number for the expanded cylinder in the steady flow regime ($1 \le \mathrm{Re} \le 47$). Similar heat transfer expression for the tapered trapezoidal cylinder in the steady regime can be found elsewhere [24, 27].

$$\bar{N}u = 0.0725 + 0.6940\,\mathrm{Re}^{0.4159} \qquad (16)$$

This correlation has a maximum deviation of less than 2.65% with the present computed results at the value of Reynolds number of 1 and Prandtl number of 0.7, which further drips down to as low as about 0.04% for Re = 20.

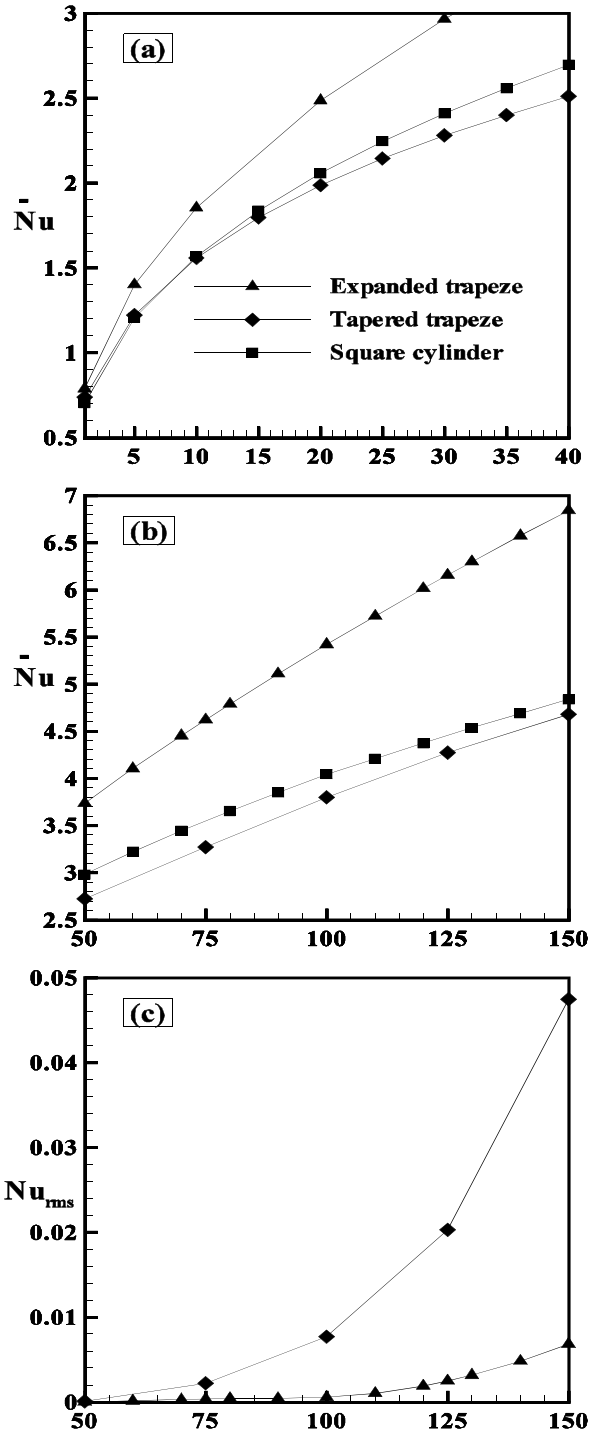

Figure 25: *Variation of the average Nusselt number (a) steady flow with the literature values of square cylinder [28] and tapered trapezoidal cylinder [24], (b) unsteady flow with the literature values of square cylinder[57] and (c) the rms values of the Nusselt number with the literature values of tapered trapezoidal cylinder[24] with Reynolds number at Pr=0.7*

Another correlative relationship (equation 17) has also been established between the values of average Nusselt number and that of Reynolds number in the unsteady periodic regime ($48 \le \mathrm{Re} \le 150$).

$$\bar{N}u = 0.424\,\mathrm{Re}^{0.553} \qquad (17)$$

The values of the average Nusselt number obtained from the above empirical equation for the corresponding values of Reynolds number recorded a maximum deviation of about 1.24% for Re = 50 and a very low value of only about 1.0% for the last point of domain of our present study, i.e. at Re = 150.

Part 2: The variation of the local Nusselt number for a trapezoidal obstacle is found to be symmetric for top and bottom halves. The value of the local Nusselt number decreases on top and bottom surfaces, i.e. from A to B and from D to C, and then increases sharply towards the rear corners B and C, respectively. On front and rear surfaces of a trapezoidal cylinder, the local minimum in the value of the local Nusselt number exists near the middle of these surfaces. The average Nusselt number ($\bar{N}u$) increases with increase in Reynolds number for a fixed value of power-law index. At constant Reynolds number, with increase in power-law index the average Nusselt number decreases. It can be inferred that shear-thinning behavior (n<1) facilitates heat transfer and shear-thickening behavior (n>1) slows it down due to a thicker boundary layer.

4.9 RMS values of drag and lift coefficients, and Nusselt number

The root mean square (RMS) values depict the measure of the amplitude of the unsteady cylinder wake oscillations and RMS values of any quantity φ can be calculated as follows:

$$\varphi_{rms} = \sqrt{\frac{\sum_{i=1}^{N}\left(\varphi_i - \varphi_{mean}\right)^2}{N}} \qquad (19)$$

where N is the total number of time steps in 10 cycles.

Figures 23(a, b) and Fig. 25(c) present the variation of RMS values of lift coefficient, drag coefficient and Nusselt number, respectively in the time-dependent regime for the case

of flow and heat transfer across an expanded trapezoidal bluff body. The variation of RMS value of lift and drag coefficients and Nusselt number for square [57] and tapered [24] cylinders with Reynolds number is also presented in these figures.

Similar to the cases of square cylinder [57] and tapered trapeze [24], the RMS values of the drag coefficients increase with the increasing value of the Reynolds number ($48 \leq \mathrm{Re} \leq 150$) in the unsteady periodic regime (Fig. 23b). The RMS value of the drag coefficient for the expanded trapezoidal cylinder is observed to be higher than both square [57] and tapered [24] cylinders for $75 < \mathrm{Re} \leq 150$. While the opposite trend is observed for the expanded cylinder than that of square cylinder [57] and of tapered one [24] for $50 \leq \mathrm{Re} < 75$; however, the differences in the values are small. The higher RMS value of the drag coefficient for the expanded trapezoidal cylinder is emphatically due to the higher amplitudes of the unsteady wake oscillations than that of square and tapered cylinders. The difference between the RMS values of the drag coefficient of expanded trapezoidal and square cylinders, and the difference between the RMS values of expanded and tapered trapeze show an increasing nature with the increasing values of the Reynolds number in the unsteady periodic regime.

Similar to the RMS value of drag, the RMS value of the lift coefficient increases with the increasing value of the Reynolds number for the range $48 \leq \mathrm{Re} \leq 150$ (Fig. 23a). However, unlike drag, the RMS values of lift coefficient for the expanded trapezoidal cylinder are observed to be lower than the tapered trapezoidal bluff body [24]. It can also be observed from the figure that the RMS values of lift coefficient of square cylinder [57] is more than that for expanded trapezoidal cylinder till Re = 100, after which an opposite trend in the RMS values of square and expanded cylinders exists for $100 < \mathrm{Re} \leq 150$ (Fig. 23a). In compliance with drag, the difference between the RMS values of tapered and expanded trapezoidal cylinders is observed to be more and follows the same trend of increasing with the increasing value of the Reynolds number in the unsteady periodic regime.

Similarly, the RMS value of the Nusselt number has also been calculated and found to increase with the increasing value of Reynolds number (Fig. 25c) for the range $48 \leq \mathrm{Re} \leq 150$ and Pr = 0.7. Unlike the higher values of the average Nusselt number for the expanded cylinder over the tapered one (Fig. 25b), the RMS values of Nusselt number however is observed to be more for the tapered trapezoidal cylinder [24] than those for the expanded trapezoidal bluff body.

4.10 Pressure Drop

The pressure loss coefficient (*dP*) for the expanded trapezoidal cylinder has been calculated by using the following simple equation (20) where Δp is the difference in the values of inlet and outlet static pressures and it has been made dimensionless by $1/2\rho U_\infty^2$ [56].

$$dP = \frac{\Delta p}{1/2\rho U_\infty^2} \tag{20}$$

Table 4: *Percentage (%) enhancement in pressure drop for the expanded trapezoidal cylinder with respect to the tapered one [24] in the steady regime*

Re	*dP*		% Enhancement w.r.t. tapered cylinder
	Expanded cylinder	Tapered cylinder	
1	13.3855	13.9508	96
5	4.9347	5.0925	97
10	3.4379	3.6181	95
20	2.4934	2.7294	91
30	2.1033	2.3992	88
40	1.8792	2.2115	85

It can be stated from Fig. 26 that the pressure drop across the expanded trapezoidal cylinder is less than that of the tapered trapezoidal cylinder. This is mainly due to the streamline shape of the expanded trapeze. It can also be observed that for both expanded and tapered cylinders, the dimensionless value of the pressure loss decreases with the increase in the value of the Reynolds number for the range of settings embraced here. Further, the pressure drop has been related to the present heat transfer results and it has been observed that, as the pressure drop decreases the heat transfer rate increases. Also, as the heat transfer increment accomplished by a pressure penalty, the enhancement in pressure drop is

calculated at different values of Reynolds numbers (Table 4). The maximum enhancement in pressure loss for the expanded trapezoidal cylinder as compared with the tapered one is found to be approximately 97% in the steady regime.

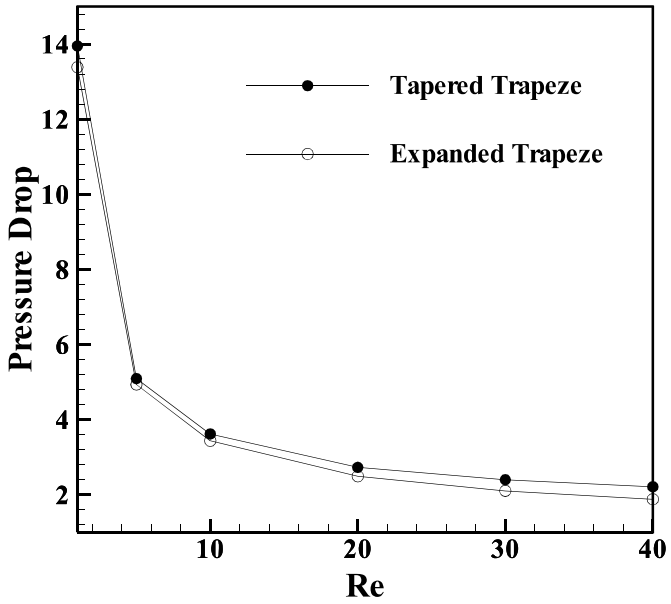

Figure 26: *Variation of pressure loss along with the values of tapered trapezoidal cylinder [24] with the Reynolds number*

CHAPTER – 5

CONCLUSIONS

Part 1: Two-dimensional flow and heat transfer across a long expanded trapezoidal cylinder in the unconfined steady and unsteady regimes are explored for Re = 1 – 150 and Pr = 0.7.

- The wake length increases with the increasing Reynolds number in the steady regime ($1 \le \mathrm{Re} \le 47$).
- The transition from steady to time-dependent regime occurs between Re = 47 and 48.
- The total drag coefficient decreases with the increasing value of the Reynolds number up to Re = 90 and thereafter it increases with Re; however, the heat transfer as well as the Strouhal number increase with the increasing value of Re.
- Simple correlations of wake length, drag, average Nusselt number and Strouhal number as a function of Reynolds number are established.
- The maximum augmentation in heat transfer for the expanded trapeze is found to be approximately 146% and 141% respectively as compared to the tapered and the square cylinders. On the other hand, the pressure drop shows an enhancement of approximately 97% for the expanded trapezoidal cylinder when compared with the tapered one.

Part 2: Forced convection momentum and heat transfer of non-Newtonian power-law fluids around a long trapezoidal bar are investigatedin the range of Reynolds number $1 \le \mathrm{Re} \le 40$ and power-law index $0.4 \le n \le 1.8$ in an unconfined domain.

- The wake length increases with increase in Reynolds number.
- As expected, with increase in Reynolds number the drag coefficient decreases in the steady regime.
- The average Nusselt number increases with increase in Reynolds number; however, it decreases with increase in power-law index.
- Similar to a long square bar, shear-thinning behavior ($n < 1$) facilitates heat transfer and shear-thickening behavior ($n > 1$) slows it down due to a thicker boundary layer.

References

[1] Pankanin, G. L., 2005, The vortex flow meter: various methods of investigating phenomena, Meas. Sci. Technol., 16: R1 – R16.

[2] Xing, J., Zhang, T., Hu, Y., 2008, Optimization of the bluff body in vortex flow meter, Proc. 7th World Congress on Intelligent Control and Automation, Chongqing, China.

[3] Venugopal, A., Agarwal, A., Prabhu, S.V., 2010, Influence of blockage and upstream disturbances on the performance of a vortex flow meter with a trapezoidal bluff, Measurement, 43 : 603 - 616.

[4] Mack, Y., Goel, T., Wae, S. Raphael, H., 2005, Multiple surrogates for the shape optimization of bluff body-facilitated mixing, Proc. 43rd AIAA Aerospace Sciences Meeting and Exhibit, Reno, Nevada.

[5] Wang, D., Pham, H., Chao, C., Chen, J.M., 2011, A piezoelectric energy harvester based on pressure fluctuations in Karman vortex street, World Renewable Energy Congress, Linkoping, Sweden.

[6] Gee, A.H., Houghton, N.E., Treece, G.M., Prager, R.W., 2005, A mechanical instrument for 3d ultrasound probe calibration, Ultrasound Med. Biol., 31: 505–518.

[7] Anderson, John D. (2004), Introduction to Flight, Section 4.20 (5th edition)

[8] Clancy, L.J., Aerodynamics, Section 4.14

[9] Balmer, David. "Separation of Boundary Layers."School of Engineering and Electronics. 2 December 2007. University of Edinburgh. 12 March 2008

[10] Barnes, Howard A. (1997). "Thixotropy a review". J. Non-Newtonian Fluid Mech., 70: 3.

[11] G. K. Batchelor (2000) [1967].An Introduction to Fluid Dynamics.Cambridge Mathematical Library series, Cambridge University Press.ISBN 0-521-66396-2.

[12] Kundu P and Cohen I. Fluid Mechanics.

[13] Kirby, B.J. (2010). Micro- and Nanoscale Fluid Mechanics: Transport in Microfluidic Devices..Cambridge University Press.ISBN 978-0-521-11903-0.

[14] Steggel N., Rockliff N., 1997, Simulations on the effects of body shape on lock in characteristics in pulsating flow by the discrete vortex method, J. Wind Eng. Ind. Aerodyn., 69-71: 317-321.

[15] Singha A., Balachandra R., 2011, Coherent structure statistics in the wake of a sharp-edged bluff body placed vertically in a shallow channel, Fluid Dyn. Res., 43: 055504-26.

[16] Goujon-Durand S., Renffer K., Wesfreid J. E., 1994, Downstream evolution of the Bernard von Karman instability, Phy. Rev. E, 50: 308 - 313.

[17] Hulin, J.P., Fierfort, C., Coudol, R., 1982, Experimental study of vortex emission behind bluff obstacles in a gas liquid vertical two-phase flow, Int. J. Multiphase Flow, 8: 475 - 490.

[18] Lee T.S., 1998, Early stages of an impulsively started unsteady laminar flow past tapered trapezoidal cylinders, Int. J. Numer. Methods Fluids, 26: 1181-203.

[19] Miau, J.J., Wang, J.T., Chou, J.H., Wei, C.Y., 2003, Low-frequency fluctuations in the near-wake region of a trapezoidal cylinder with low aspect ratio, J. Fluids Structures, 17: 701 - 715.

[20] Chung, Y.J., Kang, S.-H., 2000, Laminar vortex shedding from a trapezoidal cylinder with different height ratios, Phy. Fluids, 12: 1251 -1254.

[21] El Wahed, A.K., Johnson, M.W., Sproston, J.L., 1993, Numerical study of vortex shedding from different shaped bluff bodies, Flow Meas. Instrum., 4: 233 - 240.

[22] Kahawita, R., Wang, P., 2002, Numerical simulation of the wake flow behind trapezoidal bluff bodies, Comp. Fluids, 31: 99-112.

[23] Venugopal, A., Agarwal, A., Prabhu, S.V., 2010, Influence of blockage and shape of a bluff body on the performance of vortex flow meter with wall pressure measurement, Measurement, 44: 954 - 964.

[24] Dhiman, A., Hasan, M., 2012, Flow and heat transfer over a trapezoidal cylinder: steady and unsteady regimes, Asia-Pacific J. Chem. Eng., In press, DOI: 10.1002/apj.1678.

[25] Lee, T.S., 1998, Numerical study of early stages of an impulsively started unsteady laminar flow past expanded trapezoidal cylinders, Int. J. Numer. Methods Heat Fluid Flow, 8: 934-95.

[26] Chen, X.B., Yu, P., Winoto, S.H., Low, H.T., 2009, Numerical analysis for the flow past a porous trapezoidal cylinder based on the stress-jump interfacial conditions, Int. J. Numer. Methods Heat Fluid Flow, 19: 223-241.

[27] Dhiman, A., Ghosh, R., 2013, Computer simulation of momentum and heat transfer across an expanded trapezoidal bluff body, Int. J. Heat Mass Transfer, 59: 338 - 352.

[28] Dhiman, A.K., Chhabra, R.P., Eswaran, V., 2006, Steady flow of power-law fluids across a square cylinder, Chem. Eng. Res. Des., 84: 300 – 310.

[29] Dhiman A. K., Chhabra R.P., Eswaran V., 2007, Heat Transfer to Power-law fluids from a heated square cylinder, Numer. Heat Transfer Part A, 52: 185 - 201.

[30] Dhiman A.K., Anjaiah, N., Chhabra, R.P., Eswaran, V., 2007, Mixed convection from a heated square cylinder to Newtonian and power-law fluids, Trans. ASME J. Fluids Eng., 129: 506 - 513.

[31] Paliwal B., Sharma A., Chhabra R.P., Eswaran V., 2003, Power-law fluid flow past a squarecylinder: momentum and heat transfer characteristics, Chem. Eng. Sc., 58: 315 - 5329.

[32] Prhashanna, A., Sahu, A.K., Chhabra, R.P., 2011, Flow of power-law fluids past an equilateral triangular cylinder: Momentum and heat transfer characteristics, Int. J. Thermal Sci., 50: 2027 - 2041.

[33] R.P. Chhabra, J.F. Richardson, Non-Newtonian Flow and Applied Rheology, 2nd edition, Butterworth-Heinemann, Oxford, 2008.

[34] R. P. Chhabra, Bubbles, Drops, and Particles in Non-Newtonian Fluids, 2nd edition, CRC Press, Boca Raton, FL, 2006.

[35] Dhiman, A.K., Chhabra, R.P., Sharma, A., Eswaran, V., 2006, Effects of Reynolds and Prandtl numbers on heat transfer across a square cylinder in the steady flow regime, Numer. Heat transfer Part A, 49: 717 – 731.

[36] Bird, R.B., Stewart, W.E., Lightfoot, E.N., 2001, Transport Phenomena, 2nd edition, Wiley, New York.

[37] ANSYS, Inc., 2009, ANSYS FLUENT 12.0 User's Guide, U.S.A.

[38] Roache, P. J., 1994, Perspective: a method for uniform reporting of grid refinement studies, J. Fluid Eng., 116: 405 – 413.

[39] Patnana, V. K., Bharti, R. P., Chhabra, R. P., 2009, Two-dimensional unsteady flow of power-law fluids over a cylinder, J. Chem. Eng. Sci., 61: 6035 – 46

[40] Patnana, V. K., Bharti, R. P., Chhabra, R. P., 2010, Two-dimensional unsteady forced convection heat transfer in power-law fluids from a cylinder, Int. J. Heat Mass Transfer, 52: 4152 – 4167.

[41] Baranyi, L., 2004, Numerical simulation of flow past a cylinder in orbital motion. J. Comput. App. Mech., 5: 209 – 222.

[42] Cheng, C.-H., Hong, J.-L., Win, A., 1997. Numerical prediction of lock-on effect on convective heat transfer from a transversely oscillating circular cylinder. Int. J. Heat Mass Transfer, 40: 1825 – 1834.

[43] Mettu, S., Verma, N., Chhabra, R.P., 2006. Momentum and heat transfer from an asymmetrically confined circular cylinder in a plane channel. Heat Mass Transfer, 42: 1037 – 1046.

[44] Henderson, R.D., 1995, Details of the drag curve near the onset of vortex shedding, Phy. Fluids.7: 2102 – 2104.

[45] Sivakumar, P., Bharti, R.P., Chhabra, R.P., 2006, Effect of power-law index on critical parameters across an unconfined circular cylinder, Chem. Eng. Sci., 61: 6035 – 6046.

[46] Mittal, S., 2005. Excitation of shear layer instabilities in flow past a cylinder at low Reynolds number.Int.J. of Numer.Meth. Fluids, 49: 1147 – 1167.

[47] Clift, R., Grace, J., Weber, M.E., 1978, Bubbles, Drops and Particles, Academic Press, New York.

[48] Ding, H., Shu, C., Yeo, K.S., Xu, D., 2004. Simulation of incompressible viscous flows past a circular cylinder by hybrid FD scheme and meshless least square- based finite difference method. Comp. Meth.App. Mech. Eng., 193: 727 – 744.

[49] Liu, C., Zheng, X., Sung, C.H., 1998, Preconditioned multigrid methods for unsteady incompressible flows, J. Comput. Phy., 139: 33 – 57.

[50] Karniadakis, G.E., 1988, Numerical simulation of forced convection heat transfer from a cylinder in cross flow, Int. J. Heat Mass Transfer, 31: 107 – 118.

[51] Mahfouz, F.M., Badr, H.M., 2000, Forced convection from a rotationally oscillating cylinder placed in a uniform stream, Int. J. Heat Mass Transfer 43: 3093 – 3104.

[52] Lange, C.F., Durst, F., Breuer, M., 1998 Momentum and heat transfer from cylinder in laminar cross-flow at $10^{-4} \leq \mathrm{Re} \leq 200$, Int. J. Heat Mass Transfer 41: 3409 – 3430.

[53] Whitaker, S., 1972, Forced convection heat transfer correlations for flow in pipes, past flat plates, single cylinders, single sphere and for flow in packed beds and tube bundles, AIChE J. 18: 361 – 371.

[54] Sivakumar, P., Bharti, R.P., Chhabra, R.P., 2007, Steady flow of power-law fluids across an unconfined elliptical cylinder, Chem. Eng. Sci., 62: 1682 – 1702.

[55] Bharti, R.P., Sivakumar, P., Chhabra, R.P., 2008, Forced convection heat transfer from an elliptical cylinder to power-law fluids, Int. J. Heat Mass Transfer, 51: 1838 – 1853.

[56] Chaitanya, N. S. K., Dhiman, A. K., 2012, Non-Newtonian power-law flow and heat transfer across a pair of side-by-side circular cylinders, Int. J. heat Mass Transfer, 55: 5941 – 5958.

[57] Sharma, A., Eswaran, V., 2004, Heat and fluid flow across a square cylinder in the two-dimensional laminar flow regime, Numer. Heat Transfer A, 45: 247 - 269.